SIAM J. IMAGING SCIENCES
Vol. 7, No. 2, pp. 1080–1107

© 2014 Society for Industrial and Applied Mathematics

An Algorithm for Variable Density Sampling with Block-Constrained Acquisition[*]

Claire Boyer[†], Pierre Weiss[‡], and Jérémie Bigot[§]

Abstract. Reducing acquisition time is of fundamental importance in various imaging modalities. Variable density sampling (VDS) provides an appealing framework for addressing this issue. It was justified recently from a theoretical point of view in the compressed sensing (CS) literature. Unfortunately, the sampling schemes suggested by current CS theories may not be relevant since they do not take the acquisition constraints (for example, continuity of the acquisition trajectory in magnetic resonance imaging (MRI)) into account. In this paper, we propose a numerical method to perform variable density sampling with block constraints. Our main contribution is a new way to draw the blocks in order to mimic CS strategies based on isolated measurements. The basic idea is to minimize a tailored dissimilarity measure between a probability distribution defined on the set of isolated measurements and a probability distribution defined on a set of blocks of measurements. This problem turns out to be convex and solvable in high dimension. Our second contribution is to define an efficient minimization algorithm based on Nesterov's accelerated gradient descent in metric spaces. We carefully study the choice of the metrics and of the prox-function. We show that the optimal choice may depend on the type of blocks under consideration. Finally, we show that we can obtain better MRI reconstruction results using our sampling schemes than with standard strategies such as equiangularly distributed radial lines.

Key words. compressed sensing, blocks of measurements, block-constrained acquisition, dissimilarity measure between discrete probabilities, optimization on metric spaces

AMS subject classifications. 94A20, 90C25, 49N45, 65K10, 49M29, 49N15, 28C99

DOI. 10.1137/130941560

---

1. Introduction.

Compressive sensing (CS) is a recently developed sampling theory that provides theoretical conditions for ensuring the exact recovery of signals from a small number of linear measurements (below the Nyquist rate). CS is based on the assumption that the signal to be reconstructed can be represented by a small number of atoms in a certain basis. We say that the signal $\boldsymbol{x} \in \mathbb{C}^n$ is s-sparse if

$$\|\boldsymbol{x}\|_{\ell^0} \leq s,$$

where $\|\cdot\|_{\ell^0}$ denotes the ℓ^0 pseudonorm, counting the number of nonzero entries of $\boldsymbol{x}$. Original CS theorems [Don06, CRT06, CP11a] assert that a sparse signal $\boldsymbol{x}$ can be faithfully

---

[*] Received by the editors October 17, 2013; accepted for publication (in revised form) February 24, 2014; published electronically May 29, 2014. This work was partially supported by the CIMI (Centre International de Mathématiques et d'Informatique) Excellence program, by ANR SPH-IM-3D (ANR-12-BSV5-0008), by the FMJH Program Gaspard Monge in optimization and operation research, and by the support to that program from EDF.
http://www.siam.org/journals/siims/7-2/94156.html

[†] Institut de Mathématiques de Toulouse, Université de Toulouse, Toulouse F-31062, France (claire.boyer@math.univ-toulouse.fr).

[‡] Institut des Technologies Avancées du Vivant, Toulouse F-31062, France (pierre.armand.weiss@gmail.com).

[§] DMIA, Institut Supérieur de l'Aéronautique et de l'Espace, Toulouse F-31062, France (jeremie.bigot@isae.fr).

reconstructed via ℓ^1-minimization:

$$\min_{\boldsymbol{z}\in\mathbb{C}^n} \|\boldsymbol{z}\|_{\ell^1} \qquad \text{such that} \quad \boldsymbol{A}_\Omega \boldsymbol{z} = \boldsymbol{y}, \tag{1}$$

where $\boldsymbol{A}_\Omega \in \mathbb{C}^{p\times n}$ $(p \leq n)$ is a sensing matrix, $\boldsymbol{y} = \boldsymbol{A}_\Omega \boldsymbol{x} \in \mathbb{C}^p$ represents the vector of linear projections, and $\|\boldsymbol{z}\|_{\ell^1} = \sum_{i=1}^n |z_i|$ for all $\boldsymbol{z} = (z_1, \dots, z_n) \in \mathbb{C}^n$. More precisely, CS results state that $p = O(s\ln(n))$ measurements are enough to guarantee exact reconstruction, provided that $\boldsymbol{A}_\Omega$ satisfies some incoherence property.

One way to construct $\boldsymbol{A}_\Omega$ is by randomly extracting rows from a full sensing matrix $\boldsymbol{A} \in \mathbb{C}^{n\times n}$ that can be written as

$$\boldsymbol{A} = \begin{pmatrix} \boldsymbol{a}_1^* \\ \vdots \\ \boldsymbol{a}_n^* \end{pmatrix}, \tag{2}$$

where $\boldsymbol{a}_i^*$ denotes the ith row of $\boldsymbol{A}$. In the context of magnetic resonance imaging (MRI), for instance, the full sensing matrix $\boldsymbol{A}$ consists of the composition of a Fourier transform with an inverse wavelet transform. This choice is due to the fact that the acquisition is done in the Fourier domain, while the images to be reconstructed are assumed to be sparse in the wavelet domain. In this setting, a fundamental issue is constructing $\boldsymbol{A}_\Omega$ by extracting appropriate rows from the full sensing matrix $\boldsymbol{A}$. A theoretically founded approach to building $\boldsymbol{A}_\Omega$ (i.e., constructing sampling schemes) consists of randomly extracting rows from $\boldsymbol{A}$ according to a given density. This approach requires us to define a discrete probability distribution $\boldsymbol{p} = (\boldsymbol{p}_i)_{1\leq i\leq n}$ on the set of integers $\{1, \dots, n\}$ that represents the indexes of the rows of $\boldsymbol{A}$. We call this procedure variable density sampling. This term appeared in the early MRI paper [SPM95]. It was recently given a mathematical definition in [CCKW13]. One possibility for constructing $\boldsymbol{p}$ is to choose its ith component $\boldsymbol{p}_i$ to be proportional to $\|\boldsymbol{a}_i^*\|_{\ell^\infty}^2$ (see [Rau10, PVW11, BBW13, CCW13]); i.e.,

$$\boldsymbol{p}_i = \frac{\|\boldsymbol{a}_i^*\|_{\ell^\infty}^2}{\sum_{k=1}^n \|\boldsymbol{a}_k^*\|_{\ell^\infty}^2}, \qquad i = 1, \dots, n. \tag{3}$$

In the MRI setting, another strategy ensuring good reconstruction is to choose $\boldsymbol{p}$ according to a polynomial radial distribution [KW12] in the so-called *k-space*, i.e., the 2D Fourier plane where low frequencies are centered. Other strategies are possible. For example, [AHPR13] propose a multilevel uniformly random subsampling approach.

All these strategies lead to sampling schemes that are made of a few but isolated measurements; see, e.g., Figure 1(a). However, in many applications, the number of measurements is not of primary importance relative to the path the sensor must take to collect the measurements. For instance, in MRI, sampling is done in the Fourier domain along continuous and smooth curves [Wri97, LKP08]. Another example of the need to sample continuous trajectories can be found in mobile robots monitoring, where robots have to spatially sample their environment under kinematic and energy-consumption constraints [HPH$^+$11].

This paper focuses on the acquisition of linear measurements in applications where the physics of the sensing device allows sampling of a signal from predefined blocks of measurements. We define a block of measurements as an arbitrary set of isolated measurements, which

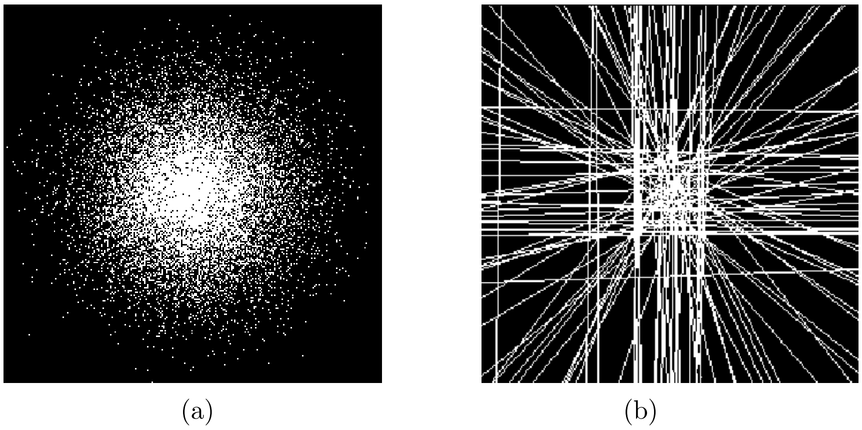

Figure 1. *An example of MRI sampling schemes in the k-space (the* 2*D Fourier plane where low frequencies are centered).* (a) *Isolated measurements drawn from a probability measure* $\boldsymbol{p}$ *having a radial distribution.* (b) *Sampling scheme based on a dictionary of blocks of measurements: blocks consist of discrete lines of the same size.*

could be contiguous in the Fourier plane, for instance. As an illustrative example (which will be used throughout the paper), one may consider sampling patterns generated by randomly drawing a set of straight lines in the Fourier plane or *k-space*, as displayed in Figure 1(b). This kind of sampling pattern is particularly relevant in the case of MRI acquisition with echo planar sampling strategies; see, e.g., [LDSP08].

Acquiring data by blocks of measurements raises the issue of designing appropriate sampling schemes. In this paper, we propose randomly extracting blocks of measurements that are made up of several rows from the full sensing matrix $\boldsymbol{A}$. The main question investigated is how to choose an appropriate probability distribution from which to draw blocks of measurements. A first step in this direction was recently proposed [BBW13, PDG12]. In [BBW13], we derived a theoretical probability distribution in the case of blocks of measurements in order to design a sensing matrix $\boldsymbol{A}_\Omega$ that guarantees an exact reconstruction of s-sparse signals with high probability. Unfortunately, the probability distributions proposed in [BBW13] and [PDG12] are difficult to compute numerically and seem suboptimal in practice.

In this paper, we propose an alternative strategy which is based on the numerical resolution of an optimization problem. Our main idea is to construct a probability distribution $\boldsymbol{\pi}$ on a dictionary of blocks. The blocks are drawn independently at random according to this distribution. We propose choosing $\boldsymbol{\pi}$ in such a way that the resulting sampling patterns are similar to those based on isolated measurements, such as those proposed in the CS literature. For this purpose, we define a dissimilarity measure to compare a probability distribution $\boldsymbol{\pi}$ on a dictionary of blocks and a target probability distribution $\boldsymbol{p}$ defined on a set of isolated measurements. Then, we propose to choose an appropriate distribution $\boldsymbol{\pi}\left[\boldsymbol{p}\right]$ by minimizing its dissimilarity from a distribution $\boldsymbol{p}$ on isolated measurements that is known to lead to good sensing matrices.

This paper is organized as follows. In section 2, we introduce the notation. In section 3, we describe the problem setting. Then, we construct a dissimilarity measure between probability distributions lying in different, but spatially related, domains. We then formulate the problem of finding a probability distribution $\boldsymbol{\pi}\left[\boldsymbol{p}\right]$ on blocks of measurements as a convex optimization problem. In section 4, we present an original and efficient way to solve this minimization problem via a dual formulation and an algorithm based on the accelerated gradient descents in metric spaces [Nes05]. We carefully study how the theoretical rates of convergence are affected by the choice of norms and prox-functions on the primal and dual spaces. Finally, in section 5, we propose a dictionary of blocks that is appropriate for MRI applications. Then, we compare the quality of MRI image reconstructions obtained using the proposed sampling schemes with those obtained via methods currently used in the context of MRI acquisition, demonstrating the potential of the proposed approach on real scanners.

2. Notation.

We consider d-dimensional signals for any $d \in \mathbb{N}^*$, of size $n_1 \times n_2 \times \cdots \times n_d = n$. Let E and F denote finite-dimensional vector spaces endowed with their respective norms $\|.\|_E$ and $\|.\|_F$. In the paper, $E = \mathbb{R}^m$ and $F = \mathbb{R}^n$. We denote by E^* and F^*, respectively, the dual spaces of E and F. For $s \in E^*$ and $x \in E$ we denote by $\langle s, x\rangle_{E^*\times E}$ the value of s at x. The notation $\langle \cdot, \cdot \rangle$ will denote the usual inner product in a Euclidean space. The norm of the dual space E^* is defined by

$$\|s\|_{E^*} = \max_{\substack{x\in E\\ \|x\|_E=1}} \langle s, x\rangle_{E^*\times E}\,.$$

Let $\boldsymbol{M} : E \to F^*$ denote some operator. When M is linear, we denote its adjoint operator by $\boldsymbol{M}^* : F \to E^*$. The subordinate operator norm is defined by

$$\|\boldsymbol{M}\|_{E\to F^*} = \sup_{\|x\|_E \le 1} \|\boldsymbol{M}x\|_{F^*}.$$

When the spaces E^* and F are endowed with ℓ^q and ℓ^p norms, respectively, we will use the following notation for the operator norm of $\boldsymbol{M}^*$:

$$\|\boldsymbol{M}^*\|_{F\to E^*} = \|\boldsymbol{M}^*\|_{p\to q}.$$

We set $\Delta_m \subset E$ to be the simplex in $E = \mathbb{R}^m$, and $\Delta_n \subset F$ to be the simplex in $F = \mathbb{R}^n$. For $\boldsymbol{\pi} \in \Delta_m$ and an index $j \in \{1, \ldots, m\}$ we denote by $\boldsymbol{\pi}_j$ the jth component of $\boldsymbol{\pi}$.

Let $g : \mathbb{R}^n \to \mathbb{R} \cup \{+\infty\}$ denote a closed convex function. Its Fenchel conjugate is denoted g^*. The relative interior of a set $X \subseteq \mathbb{R}^n$ is denoted $\mathrm{ri}(X)$. Finally, the normal cone to X at a point x on the boundary of X is denoted $\mathcal{N}_X(x)$.

3. Variable density sampling with block constraints.

3.1. Problem setting.

In this paper, we assume that the acquisition system is capable of sensing a finite set $\{y_1, \ldots, y_n\}$ of linear measurements of a signal $\boldsymbol{x} \in \mathbb{R}^{n_s}$ such that

$$y_i = \langle \boldsymbol{a}_i^*, \boldsymbol{x}\rangle \qquad \forall i = 1, \ldots, n,$$

where $\boldsymbol{a}_i^*$ denotes the ith row of the full sensing matrix $\boldsymbol{A}$. Let us define a set $\mathcal{I} = \{I_1, \ldots, I_m\}$, where each $I_k \subseteq \{1, \ldots, n\}$ denotes a set of indexes. We assume that the acquisition system has physical constraints that impose sensing the following sets of measurements:

$$E_k = \{y_i, i \in I_k\} \qquad \forall k = 1, \ldots, m.$$

In what follows, we refer to $\mathcal{I}$ as the blocks dictionary.

For example, in MRI, $n = n_s$ is the number of pixels or voxels of a 2D or 3D image, and y_i represents the ith discrete Fourier coefficient of this image. In this setting, the sets of indexes I_k may represent straight lines in the discrete Fourier domain, as in Figure 1(b). In section 5.1, we give further details on the construction of such a dictionary.

We propose to partially sense the signal using the following procedure:

(i) Construct a discrete probability distribution $\boldsymbol{\pi} \in \Delta_m$.

(ii) Draw i.i.d. (independent and identically distributed) indexes $k_1, \dots, k_b$ from the probability distribution $\boldsymbol{\pi}$ on the set $\{1, \dots, m\}$, with $1 \leq b \leq m$.

(iii) Sense the signal $\boldsymbol{x}$ randomly by considering the random set of blocks of measurements $(E_{k_j})_{j\in\{1,\dots,b\}}$, which leads to the construction of the following sensing matrix:

$$\boldsymbol{A}_\Omega = (\boldsymbol{a}_i^*)_{i \in \cup_{j=1}^b I_{k_j}} .$$

The main objective of this paper is to provide an algorithm for constructing the discrete probability distribution $\boldsymbol{\pi}$ based on the knowledge of a target discrete probability distribution $\boldsymbol{p} \in \Delta_n$ on the set $\{y_1, \dots, y_n\}$ of isolated measurements. The problem of choosing a distribution $\boldsymbol{p}$ that will lead to good image reconstruction is not addressed in this paper, since there already exist various theoretical results and heuristic strategies in the CS literature on that topic [LKP08, CCW13, AHPR13, KW12].

3.2. A variational formulation. In order to define $\boldsymbol{\pi}$, we propose minimizing a dissimilarity measure between $\boldsymbol{\pi} \in \Delta_m$ and $\boldsymbol{p} \in \Delta_n$. The difficulty lies in the fact that these two probability distributions belong to different spaces. We propose constructing a dissimilarity measure $\mathcal{D}(\boldsymbol{\pi}, \boldsymbol{p}, \mathcal{I})$ that depends on the blocks dictionary $\mathcal{I}$. This dissimilarity measure will be minimized over $\boldsymbol{\pi} \in \Delta_m$ using numerical algorithms, with m being relatively large (typically $10^4 \leq m \leq 10^{10}$). Therefore, it must have appropriate properties, such as convexity, for the problem to be solvable in an efficient way.

3.2.1. Mapping the m-dimensional simplex to the n-dimensional one. In order to define a reasonable dissimilarity measure, we propose constructing an operator $\boldsymbol{M}$, which maps a probability distribution $\boldsymbol{\pi} \in \Delta_m$ to some $\boldsymbol{p}' \in \Delta_n$:

$$\begin{aligned} \boldsymbol{M} : \qquad & E \longrightarrow F^*, \\ & \boldsymbol{\pi} \longmapsto \boldsymbol{p}', \end{aligned}$$

where for $i \in \{1, \dots, n\}$

$$\boldsymbol{p}'_i = \frac{\sum_{k=1}^m \boldsymbol{\pi}_k \mathbb{1}_{i \in I_k}}{\sum_{j=1}^n \sum_{k'=1}^m \boldsymbol{\pi}_{k'} \mathbb{1}_{j \in I_{k'}}}, \tag{4}$$

where $\mathbb{1}_{i \in I_k}$ is equal to 1 if $i \in I_k$, and 0 otherwise. The ith element of $\boldsymbol{p}'$ represents the probability of drawing the ith measurement y_i by drawing blocks of measurements according to the probability distribution $\boldsymbol{\pi}$. The operator $\boldsymbol{M}$ satisfies the following property by construction:

$$\boldsymbol{M} \Delta_m \subseteq \Delta_n.$$

3.2.2. A sufficient condition for the mapping M to be a linear operator. Note that the operator $\boldsymbol{M}$ is generally nonlinear, due to the denominator in (4). This is usually an important drawback for the design of numerical algorithms involving the operator $\boldsymbol{M}$. However, if the sets $(I_k)_{k\in\{1,\dots,m\}}$ all have the same cardinality (or length) equal to ℓ, the denominator in (4) is equal to ℓ. In this case, $\boldsymbol{M}$ becomes a linear operator. In this paper, we will focus on this setting, which is rich enough for many practical applications, as seen next.

Assumption 3.1. For $k \in \{1,\dots,m\}$, $Card\,(I_k) = \ell$, where ℓ is some positive integer.

Let us provide two important results for the remainder of the paper.

Proposition 3.2. *For $\ell > 1$, $\boldsymbol{M}\Delta_m \subsetneq \Delta_n$; i.e., $\boldsymbol{M}\Delta_m$ is a strict subset of Δ_n.*

Proof. By definition of the convex envelope, $\boldsymbol{M}\Delta_m = \mathrm{conv}\,(\{\boldsymbol{M}_{:,i},\ i \in \{1,\dots,m\}\})$, where $\boldsymbol{M}_{:,i}$ denotes the ith column of $\boldsymbol{M}$. For $\ell > 1$, $\{\boldsymbol{M}_{:,i},\ i \in \{1,\dots,m\}\}$ is a subset of Δ_n that does not contain the extreme points of the simplex. ■

In practice, Proposition 3.2 means that it is impossible to reach an arbitrary distribution $\boldsymbol{p} \in \Delta_n$ exactly, except in the trivial case of isolated measurements.

Proposition 3.3. *Suppose that Assumption 3.1 holds; then for $p \in [1,\infty]$,*

$$\|\boldsymbol{M}^*\|_{p\to\infty} = \ell^{-\frac{1}{p}}.$$

Proof. Under Assumption 3.1, all the columns of $\boldsymbol{M}$ have only ℓ nonzero coefficients equal to $1/\ell$. With $\|\cdot\|_F = \|\cdot\|_{\ell^p}$, we can thus derive that

$$\begin{aligned}
\|\boldsymbol{M}^*\|_{p\to\infty} &= \max_{\|x\|_p=1} \|\boldsymbol{M}^* x\|_{\ell^\infty} = \max_{1\le i\le m}\ \max_{\|x\|_p=1} \langle \boldsymbol{M}_{:,i}, x\rangle \\
&= \max_{1\le i\le m} \|\boldsymbol{M}_{:,i}\|_{F^*} = \max_{1\le i\le m} \|\boldsymbol{M}_{:,i}\|_q \\
&= \ell^{-\frac{1}{p}},
\end{aligned}$$

where $\boldsymbol{M}_{:,i}$ denotes the ith column of $\boldsymbol{M}$ and q is the conjugate of p satisfying $1/p + 1/q = 1$. ■

3.2.3. Measuring the dissimilarity between π and p through the operator M. Now that we have introduced the mapping $\boldsymbol{M}$, we propose to define a dissimilarity measure between $\boldsymbol{\pi} \in \Delta_m$ and $\boldsymbol{p} \in \Delta_n$. To do so, we propose comparing $\boldsymbol{M\pi}$ and $\boldsymbol{p}$, which are both vectors belonging to the simplex Δ_n. Owing to Proposition 3.2, it is impossible to find some $\tilde{\boldsymbol{\pi}} \in \Delta_m$ satisfying $\boldsymbol{M}\tilde{\boldsymbol{\pi}} = \boldsymbol{p}$ for an arbitrary target density $\boldsymbol{p}$. Therefore, we can expect to get an approximate solution only by minimizing a dissimilarity measure $\mathcal{D}(\boldsymbol{M\pi}, \boldsymbol{p})$. For obvious numerical reasons, $\mathcal{D}$ should be convex in $\boldsymbol{\pi}$. Among statistical distances, the most natural ones are the total variation distance, Kullback–Leibler, or more generally f-divergences. Among this family, total variation presents the interesting feature of having a dual of bounded support. We will exploit this property in designing efficient numerical algorithms in section 4. In the rest of the paper, we will thus use $\mathcal{D}(\boldsymbol{M\pi}, \boldsymbol{p}) = \|\boldsymbol{M\pi} - \boldsymbol{p}\|_{\ell^1}$ to compare the distributions $\boldsymbol{M\pi}$ and $\boldsymbol{p}$.

3.2.4. Entropic regularization. In applications such as MRI, the number m of columns of $\boldsymbol{M}$ is larger than the number n of its rows. Therefore, $\mathrm{Ker}(\boldsymbol{M}) \neq \emptyset$, and there exist multiple

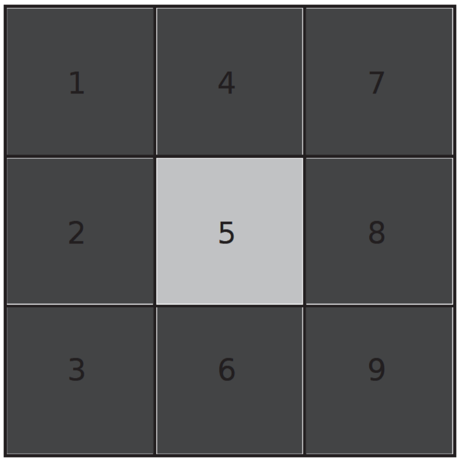

Figure 2. *Illustration of a target distribution concentrated on the central pixel of a* 3×3 *image. The pixels are numbered, and this order is kept in the design of* $\boldsymbol{M}$ *and* $\boldsymbol{\pi}$*.*

$\boldsymbol{\pi} \in \Delta_m$ with the same dissimilarity measure $\mathcal{D}(\boldsymbol{M}\boldsymbol{\pi}, \boldsymbol{p})$. In this case, we propose to take, among all these solutions, the one minimizing the neg-entropy $\mathcal{E}$ defined by

$$\mathcal{E} : \boldsymbol{\pi} \in \Delta_m \longmapsto \sum_{j=1}^{m} \boldsymbol{\pi}_j \log(\boldsymbol{\pi}_j), \tag{5}$$

with the convention that $0 \log(0) = 0$. We recall that the entropy $\mathcal{E}(\boldsymbol{\pi})$ is proportional to the Kullback–Leibler divergence between $\boldsymbol{\pi}$ and the uniform distribution $\boldsymbol{\pi}^c$ in Δ_m (i.e., such that $\boldsymbol{\pi}^c_j = \frac{1}{m}$ for all j). Therefore, among all the solutions minimizing $\mathcal{D}(\boldsymbol{M}\boldsymbol{\pi}, \boldsymbol{p})$, choosing the distribution $\boldsymbol{\pi}(\boldsymbol{p})$ minimizing $\mathcal{E}(\boldsymbol{\pi})$ gives priority to entropic solutions, i.e., probability distributions which maximize the covering of the sampling space if we proceed to several drawings of blocks of measurements. Therefore, we can finally write the regularized problem defined by

$$\min_{\boldsymbol{\pi} \in \Delta_m} F_\alpha(\boldsymbol{\pi}), \tag{PP}$$

where

$$F_\alpha(\boldsymbol{\pi}) = \|\boldsymbol{M}\boldsymbol{\pi} - \boldsymbol{p}\|_{\ell^1} + \alpha \mathcal{E}(\boldsymbol{\pi})$$

for some regularization parameter $\alpha > 0$. Adding the neg-entropy has the effect of spreading out the probability distribution $\boldsymbol{\pi}$, which is a desirable property. Moreover, the neg-entropy is strongly convex on the simplex Δ_m. This feature is of primary importance for the numerical resolution of the above optimization problem. Note that an appropriate choice of the regularization parameter α is also important, but this issue will not be addressed in this paper.

3.2.5. A toy example. To illustrate the interest of problem (PP), we design a simple example. Consider a 3×3 image. Define the target distribution $\boldsymbol{p}$ as a Dirac mass supported on the central pixel (numbered 5 in Figure 2). Consider a blocks dictionary composed of horizontal and vertical lines. In that setting, the operator $\boldsymbol{M}$ is given by

$$\boldsymbol{M} = \frac{1}{3}\begin{pmatrix} 1 & 0 & 0 & 0 & 1 & 0 & 0 \\ 1 & 0 & 0 & 0 & 0 & 1 & 0 \\ 1 & 0 & 0 & 0 & 0 & 0 & 1 \\ 0 & 1 & 0 & 0 & 1 & 0 & 0 \\ 0 & 1 & 0 & 0 & 0 & 1 & 0 \\ 0 & 1 & 0 & 0 & 0 & 0 & 1 \\ 0 & 0 & 1 & 0 & 1 & 0 & 0 \\ 0 & 0 & 1 & 0 & 0 & 1 & 0 \\ 0 & 0 & 1 & 0 & 0 & 0 & 1 \end{pmatrix}.$$

For such a matrix, there are various distributions minimizing $\|\boldsymbol{M}\boldsymbol{\pi} - \boldsymbol{p}\|_{\ell^1}$. For example, one can choose $\boldsymbol{\pi}_1 = \begin{pmatrix} 0 & 1 & 0 & 0 & 0 & 0 \end{pmatrix}^*$ or $\boldsymbol{\pi}_2 = \begin{pmatrix} 0 & 1/2 & 0 & 0 & 1/2 & 0 \end{pmatrix}^*$. The solution maximizing the entropy is $\boldsymbol{\pi}_2$. In the case of image processing, this solution is preferable since it leads to better covering of the acquisition space. Note that, among all the ℓ^p norms $(1 \leq p < +\infty)$, only the ℓ^1 norm is such that $\|\boldsymbol{M}\boldsymbol{\pi}_1 - \boldsymbol{p}\|_{\ell^1} = \|\boldsymbol{M}\boldsymbol{\pi}_2 - \boldsymbol{p}\|_{\ell^1}$. This property is once again desirable since we want the regularizing term (and not the fidelity term) to force choosing the proper solution.

4. Optimization.

In this section, we propose a numerical algorithm for solving problem (PP). Note that, despite being convex, this optimization problem has some particularities that make it difficult to solve. First, the parameter $\boldsymbol{\pi} \in \Delta_m$ lies in a very high-dimensional space. In our experiments, n varies between 10^4 and 10^7, while m varies between 10^4 and 10^{10}. Moreover, the function $\mathcal{E}$ is differentiable, but its gradient is not Lipschitz, and the total variation distance $\|\cdot\|_{\ell^1}$ is nondifferentiable.

The numerical resolution of problem (PP) is thus a delicate issue. Below, we propose an efficient strategy based on numerical optimization of the dual problem of (PP) and on the use of Nesterov's ideas [Nes05]. In contrast to most first-order methods proposed recently in the literature [BC11, Nes13, CDV10], which are based on Hilbert space formalisms, Nesterov's algorithm is stated in a (finite-dimensional) normed space. We thus perform the minimization of the dual problem on a metric space, and we carefully study the optimal choice of the norms in the primal and dual spaces. We show that, depending on the block length ℓ, the optimal choice might well be different from the standard ℓ^2 norm. Such ideas go back to (at least) [CT93] but have barely been used in the domain of image processing.

4.1. Dualization of the problem.

Our algorithm consists of solving the problem dual to (PP) in order to avoid the difficulties related to the nondifferentiability of the ℓ^1 norm. Propositions 4.1 and 4.3 state that the dual of problem (PP) is differentiable. We will use this feature to design an efficient first-order algorithm and use the primal-dual relationships (Proposition 4.4) to retrieve the primal solution.

Proposition 4.1. *Let* $J_\alpha(\boldsymbol{q}) := \langle \boldsymbol{p}, \boldsymbol{q} \rangle_{F^* \times F} - \alpha \log\left(\sum_{\ell=1}^m \exp\left(-\frac{(\boldsymbol{M}^*\boldsymbol{q})_\ell}{\alpha}\right)\right)$ *for* $\boldsymbol{q} \in F$. *The dual problem to* (PP) *is*

$$\text{(DP)} \qquad -\min_{\boldsymbol{q} \in B_\infty} J_\alpha(\boldsymbol{q}),$$

in the sense that $\min_{\boldsymbol{\pi}\in\Delta_m} F_\alpha(\boldsymbol{\pi}) = \max_{\boldsymbol{q}\in B_\infty} -J_\alpha(\boldsymbol{q})$*, where* B_∞ *is the* ℓ^∞*-ball of unit radius in* F*.*

Proof. The proof is given in Appendix A. ■

In order to study the regularity properties of J_α, and so the solvability of (DP), we use the strong convexity of the neg-entropy $\mathcal{E}$ w.r.t. $\|\cdot\|_E$. First, let us recall one version of the definition of the strong convexity in Banach spaces.

Definition 4.1. *We say that* $f : F \to \mathbb{R}$ *is* σ*-strongly convex w.r.t.* $\|\cdot\|_F$ *on* $F' \subset F$ *if*

$$\forall x, y \in F',\ \forall t \in [0,1], \quad f(tx + (1-t)y) \le tf(x) + (1-t)f(y) - \frac{\sigma}{2}t(1-t)\|x-y\|_F^2. \tag{6}$$

We define the convexity modulus σ_f *of* f *as the largest positive real* σ *satisfying* (6)*.*

Proposition 4.2. *For* $\|\cdot\|_E = \|\cdot\|_{\ell^p}$*,* $p \in [1, +\infty]$*, the convexity modulus of the neg-entropy on the simplex* Δ_m *is* $\sigma_{\mathcal{E}} = 1$*.*

Proof. The proof is given in Appendix B. ■

Proposition 4.3. *The function* J_α *is convex, and its gradient is Lipschitz continuous; i.e.,*

$$\|\nabla J_\alpha(\boldsymbol{q}_1) - \nabla J_\alpha(\boldsymbol{q}_2)\|_{F^*} \le L_\alpha \|\boldsymbol{q}_1 - \boldsymbol{q}_2\|_F \qquad \forall(\boldsymbol{q}_1, \boldsymbol{q}_2) \in F^2,$$

with constant

$$L_\alpha = \frac{\|\boldsymbol{M}^*\|_{F\to E^*}^2}{\alpha\sigma_{\mathcal{E}}}. \tag{7}$$

Moreover, ∇J_α *is locally Lipschitz around* $\boldsymbol{q} \in F$ *with constant*

$$L_\alpha(\boldsymbol{q}) = \frac{\|\boldsymbol{M}^*\|_{F\to E^*}^2}{\alpha\sigma_{\mathcal{E}}(\boldsymbol{\pi}(\boldsymbol{q}))}, \tag{8}$$

where $\sigma_{\mathcal{E}}(\boldsymbol{\pi}) := \inf_{\|\boldsymbol{h}\|_E=1}\langle \mathcal{E}''(\boldsymbol{\pi})\boldsymbol{h}, \boldsymbol{h}\rangle$ *is the local convexity modulus of* $\mathcal{E}$ *around* $\boldsymbol{\pi}$*, and an explicit expression for* $\boldsymbol{\pi}(\boldsymbol{q})$ *is given in* (19)*.*

Proof. The proof is given in Appendix C. ■

Note that a standard reasoning would rather lead to $L_\alpha = \frac{\|\boldsymbol{M}^*\|_{2\to 2}^2}{\alpha\sigma_{\mathcal{E}}}$, which is usually much larger than the bound (7). Proposition 4.3 implies that problem (DP) is efficiently solvable by Nesterov's algorithm [Nes05]. Therefore, we will first solve the dual problem (DP). Then, we use the relationships between the primal and dual solutions (as described in Proposition 4.4) to finally compute a primal solution $\boldsymbol{\pi}^\star$ for problem (PP).

Proposition 4.4. *The relationships between the primal and dual solutions*

$$\boldsymbol{\pi}^\star = \operatorname*{arg\,min}_{\boldsymbol{\pi}\in\Delta_m} F_\alpha(\boldsymbol{\pi}) \quad \text{and} \quad \boldsymbol{q}^\star = \operatorname*{arg\,min}_{\boldsymbol{q}\in B_\infty} J_\alpha(\boldsymbol{q})$$

are given by

$$\boldsymbol{\pi}_j^\star = \frac{\exp\left(-\frac{(\boldsymbol{M}^*\boldsymbol{q}^\star)_j}{\alpha}\right)}{\sum_{k=1}^m \exp\left(-\frac{(\boldsymbol{M}^*\boldsymbol{q}^\star)_k}{\alpha}\right)} \qquad \forall j \in \{1, \dots, m\}. \tag{9}$$

Furthermore,

$$\operatorname{sign}\left(\boldsymbol{M}\boldsymbol{\pi}^\star - \boldsymbol{p}\right) = \operatorname{sign}\left(\boldsymbol{q}^\star\right). \tag{10}$$

Proof. Equation (9) is a direct consequence of (19). To derive the second equation, (10), it suffices to write the optimality conditions of the problem $\max_{\boldsymbol{q}\in B_\infty} \langle \boldsymbol{M}\boldsymbol{\pi}^\star - \boldsymbol{p}, \boldsymbol{q}\rangle_{F^*\times F} + \alpha\mathcal{E}(\boldsymbol{\pi}^\star)$. This leads to

$$\boldsymbol{M}\boldsymbol{\pi}^\star - \boldsymbol{p} \in \mathcal{N}_{B_\infty}(\boldsymbol{q}^\star) \Leftrightarrow \operatorname{sign}\left(\boldsymbol{M}\boldsymbol{\pi}^\star - \boldsymbol{p}\right) = \operatorname{sign}\left(\boldsymbol{q}^\star\right). \qquad ■$$

4.2. Numerical optimization of the dual problem. Now that the dual problem (DP) is fully characterized, we propose to solve it using Nesterov's optimal accelerated projected gradient descent [Nes05] for smooth convex optimization.

4.2.1. The algorithm. Nesterov's algorithm is based on the choice of a prox-function d of the set B_∞, i.e., a continuous function that is strongly convex on B_∞ w.r.t. $\|\cdot\|_F$. Letting σ_d denote the convexity modulus of d, we further assume that $d(\boldsymbol{q}_c) = 0$, so that

$$d(\boldsymbol{q}) \geq \frac{\sigma_d}{2}\|\boldsymbol{q} - \boldsymbol{q}_c\|_F^2 \qquad \forall \boldsymbol{q} \in B_\infty,$$

where $\boldsymbol{q}_c = \arg\min_{\boldsymbol{q}\in B_\infty} d(\boldsymbol{q})$. Nesterov's algorithm is described in Algorithm 1.

Algorithm 1 Resolution scheme for smooth optimization proposed by [Nes05].

```
Initialization: choose $\boldsymbol{q}_0 \in B_\infty$.
for $k = 0, \dots, K$ do
    Compute $J_\alpha(\boldsymbol{q}_k)$ and $\nabla J_\alpha(\boldsymbol{q}_k)$.
    Find $\boldsymbol{y}_k \in \arg\min_{\boldsymbol{y}\in B_\infty} \langle \nabla J_\alpha(\boldsymbol{q}_k), \boldsymbol{y} - \boldsymbol{q}_k\rangle + \frac{1}{2}L_\alpha\|\boldsymbol{y} - \boldsymbol{q}_k\|_F^2$.
    Find $\boldsymbol{z}_k \in \arg\min_{\boldsymbol{q}\in B_\infty} \frac{L_\alpha}{\sigma_d}d(\boldsymbol{q}) + \sum_{i=0}^{k} \frac{i+1}{2}\left[J_\alpha(\boldsymbol{q}_i) + \langle \nabla J_\alpha(\boldsymbol{q}_i), \boldsymbol{q} - \boldsymbol{q}_i\rangle\right]$.
    Set $\boldsymbol{q}_{k+1} = \frac{2}{k+3}\boldsymbol{z}_k + \frac{k+1}{k+3}\boldsymbol{y}_k$.
end for
Set the primal solution to
    $\boldsymbol{\pi}_j = \frac{\exp\left(-\frac{(\boldsymbol{M}^*\boldsymbol{y}_K)_j}{\alpha}\right)}{\sum_{k=1}^{m}\exp\left(-\frac{(\boldsymbol{M}^*\boldsymbol{y}_K)_k}{\alpha}\right)} \qquad \forall j \in \{1, \dots, m\}.$
```

Theorem 4.5 summarizes the theoretical guarantees of Algorithm 1.

Theorem 4.5 (see [Nes05, Theorem 2]). *Algorithm 1 ensures that*

$$\begin{aligned} J_\alpha(\boldsymbol{y}_k) - J_\alpha(\boldsymbol{q}^\star) &\leq \frac{4L_\alpha d(\boldsymbol{q}^\star)}{\sigma_d(k+1)(k+2)} \\ &\leq \frac{4\|\boldsymbol{M}^*\|_{F\to E^*}^2 d(\boldsymbol{q}^\star)}{\alpha\sigma_{\mathcal{E}}\sigma_d(k+1)(k+2)}, \end{aligned} \tag{11}$$

where $\boldsymbol{q}^\star$ is an optimal solution of problem (DP)*.*

Since $d(\boldsymbol{q}^\star)$ is generally unknown, we can bound (11) by

$$\frac{4\|\boldsymbol{M}^*\|^2_{F\to E^*}D}{\alpha\sigma_{\mathcal{E}}\sigma_d(k+1)(k+2)}, \tag{12}$$

where $D = \max_{\boldsymbol{q}\in B_\infty} d(\boldsymbol{q})$. Note that, until now, we got theoretical guarantees in the dual space but not in the primal. What matters to us is rather to obtain guarantees on the primal iterates, which can be summarized by the following theorem.

Theorem 4.6. *Define*

$$\boldsymbol{\pi}_k = \frac{\exp\left(-\frac{(\boldsymbol{M}^*\boldsymbol{y}_k)}{\alpha}\right)}{\left\|\exp\left(-\frac{(\boldsymbol{M}^*\boldsymbol{y}_k)}{\alpha}\right)\right\|_{\ell^1}},$$

where $\boldsymbol{y}_k$ is defined in Algorithm 1. The following inequality holds:

$$\|\boldsymbol{\pi}_k - \boldsymbol{\pi}^\star\|^2_E \le \frac{8\|\boldsymbol{M}^*\|^2_{F\to E^*}D}{\alpha^2\sigma^2_{\mathcal{E}}\sigma_d(k+1)(k+2)}.$$

The proof is given in Appendix D. It is a direct consequence of a more general result of independent interest.

4.2.2. Choosing the prox-function and the metrics.

Algorithm 1 depends on the choice of $\|\cdot\|_E$, $\|\cdot\|_F$, and d. The usual accelerated projected gradient descents consist of setting $\|\cdot\|_E = \|\cdot\|_{\ell^2}$, $\|\cdot\|_F = \|\cdot\|_{\ell^2}$, and $d(\cdot) = \frac{1}{2}\|\cdot\|^2_{\ell^2}$. However, we will see that it is possible to change the algorithm's speed of convergence by making a different choice. In this paper we concentrate on the usual ℓ^p norms, $p \in [1, +\infty]$.

Choosing a norm on E. The following proposition shows an optimal choice for $\|\cdot\|_{E^*}$.

Proposition 4.7. *The norm $\|\cdot\|_{E^*}$ that minimizes (12) among all ℓ^p norms, $p \in [1, +\infty]$, is $\|\cdot\|_{\ell^\infty}$. Note, however, that the minimum local Lipschitz constant $L_\alpha(\boldsymbol{q})$ for $\boldsymbol{q} \in F$ might be reached for another choice of $\|\cdot\|_{E^*}$.*

Proof. From Proposition 4.2, we get that $\sigma_{\mathcal{E}}$ remains unchanged no matter how $\|\cdot\|_E$ is chosen among ℓ^p norms. The choice of $\|\cdot\|_E$ is thus driven by the minimization of $\|\boldsymbol{M}^*\|_{F\to E^*}$. From the operator norm definition, it is clear that the best choice consists of setting $\|\cdot\|_{E^*} = \|\cdot\|_{\ell^\infty}$, since the ℓ^∞ norm is the smallest of all ℓ^p norms. ■

According to Proposition 4.7, choosing $\|\cdot\|_{E^*}$ to be $\|\cdot\|_{\ell^\infty}$ leads to considering $\|\cdot\|_E$ to be $\|\cdot\|_{\ell^1}$. As shown by Proposition 3.3, it is clear that the norm $\|\boldsymbol{M}^*\|_{F\to E^*}$ may vary a lot w.r.t. $\|\cdot\|_F$ for the particular operator $\boldsymbol{M}$ considered in this paper.

Choosing a norm on $\boldsymbol{F}$ and a prox-function $\boldsymbol{d}$. By Proposition 4.7, the norm $\|\cdot\|_F$ and the prox-function d should be chosen in order to minimize $\frac{\|\boldsymbol{M}^*\|^2_{F\to\infty}D}{\sigma_d}$. We are unaware of a general theory for making an optimal choice, despite recent progress in that direction. The recent paper [dJ13] proposes a systematic way of selecting $\|\cdot\|_F$ and d in order to make the algorithm complexity invariant to change of coordinates for a general optimization problem. The general idea in [dJ13] is to choose $\|\cdot\|_F$ to be the Minkowski gauge of the constraints set (of the optimization problem), and d to be a strongly convex approximation of $\frac{1}{2}\|\cdot\|^2_F$. However, this strategy has not been shown to be optimal. In our setting, since the constraints set is B_∞, this would lead to choosing $\|\cdot\|_F = \|\cdot\|_{\ell^\infty}$. Unfortunately, there is no good strongly convex approximation of $\frac{1}{2}\|\cdot\|_{\ell^\infty}^2$.

In this paper, we thus study the influence of $\|\cdot\|_F$ and d both theoretically and experimentally, with $\|\cdot\|_F \in \{\|\cdot\|_{\ell^1}, \|\cdot\|_{\ell^2}, \|\cdot\|_{\ell^\infty}\}$. Propositions 4.8, 4.9, and 4.10 summarize the theoretical algorithmic complexity in different regimes.

Proposition 4.8. *Let $p' \in]1,2]$. Define $d_{p'}(x) = \frac{1}{2}\|x\|_{p'}^2$. Then the following hold:*

- *For $p \in [p', \infty]$, $d_{p'}$ is $(p'-1)$-strongly convex w.r.t. $\|\cdot\|_p$.*
- *For $p \in [1, p']$, $d_{p'}$ is $(p'-1)n^{(1/p'-1/p)}$-strongly convex w.r.t. $\|\cdot\|_p$.*

Proof. The proof is a direct consequence of [JN08, Proposition 3.6] and of the fact that, for $p' \geq p$,

$$\|x\|_{p'} \leq \|x\|_p \leq n^{(1/p-1/p')}\|x\|_{p'}. \qquad \blacksquare$$

Proposition 4.9. *Suppose that Assumption 3.1 holds. Set $\|\cdot\|_F = \|\cdot\|_p$ and $d = d_{p'}$ with $p \in [1, \infty]$ and $p' \in]1,2]$. For all this family of norms and prox-functions, the choice minimizing the complexity bound (12) is*

- *$p' = 2$ and $p \in [1,2]$ if $\ell^2 = n$. For this choice, we get*

$$J_\alpha(\boldsymbol{y}_k) - J_\alpha(\boldsymbol{q}^\star) \leq \frac{2\sqrt{n}}{\alpha(k+1)(k+2)}. \tag{13}$$

- *$p = p' = 2$ if $\ell^2 < n$. For this choice, we get*

$$J_\alpha(\boldsymbol{y}_k) - J_\alpha(\boldsymbol{q}^\star) \leq \frac{2n}{\alpha\ell(k+1)(k+2)}. \tag{14}$$

- *$p = 1$ and $p' = 2$ if $\ell^2 > n$. For this choice, we get*

$$J_\alpha(\boldsymbol{y}_k) - J_\alpha(\boldsymbol{q}^\star) \leq \frac{2n^{3/2}}{\alpha\ell^2(k+1)(k+2)}. \tag{15}$$

Proof. The result is a direct consequence of Proposition 4.8. $\blacksquare$

Unfortunately, the bounds in (13), (14), and (15) are dimension dependent. Moreover, the optimal choice suggested by Proposition 4.9 is different from the Minkowski gauge approach suggested in [dJ13]. Indeed, in all the cases described in Proposition 4.5, the optimal choice $\|\cdot\|_F$ differs from $\|\cdot\|_{\ell^\infty}$. The difficulty in applying this approach is in finding a function $d \simeq 1/2\|\cdot\|_{\ell^\infty}^2$-strongly convex w.r.t. $\|\cdot\|_{\ell^\infty}$. A simple choice consists of setting $d_\varepsilon = \frac{1}{2}\|\cdot\|_{\ell^\infty}^2 + \frac{\varepsilon}{2}\|\cdot\|_{\ell^2}^2$. This function is ε-strongly convex w.r.t. $\|\cdot\|_{\ell^\infty}$. We thus get the following proposition.

Proposition 4.10. *Suppose that Assumption 3.1 holds, with $\ell = \sqrt{n}$. Set $\|\cdot\|_F = \|\cdot\|_{\ell^\infty}$, $d_\varepsilon(\cdot) = \frac{1}{2}\|\cdot\|_{\ell^\infty}^2 + \frac{\varepsilon}{2}\|\cdot\|_{\ell^2}^2$. Then*

$$J_\alpha(\boldsymbol{y}_k) - J_\alpha(\boldsymbol{q}^\star) \leq \frac{2\,(1/\varepsilon + n)}{\alpha(k+1)(k+2)}.$$

In particular, for $\varepsilon \propto \frac{1}{n}$, $J_\alpha(\boldsymbol{y}_k) - J_\alpha(\boldsymbol{q}^\star) = O\left(\frac{n}{\alpha k^2}\right)$.

Note that this complexity bound is worse than that of Proposition 4.9 in the case where $\ell = \sqrt{n}$. In the next section, we intend to illustrate and to confirm in practice the different rates of convergence predicted by the theoretical results of Proposition 4.9.

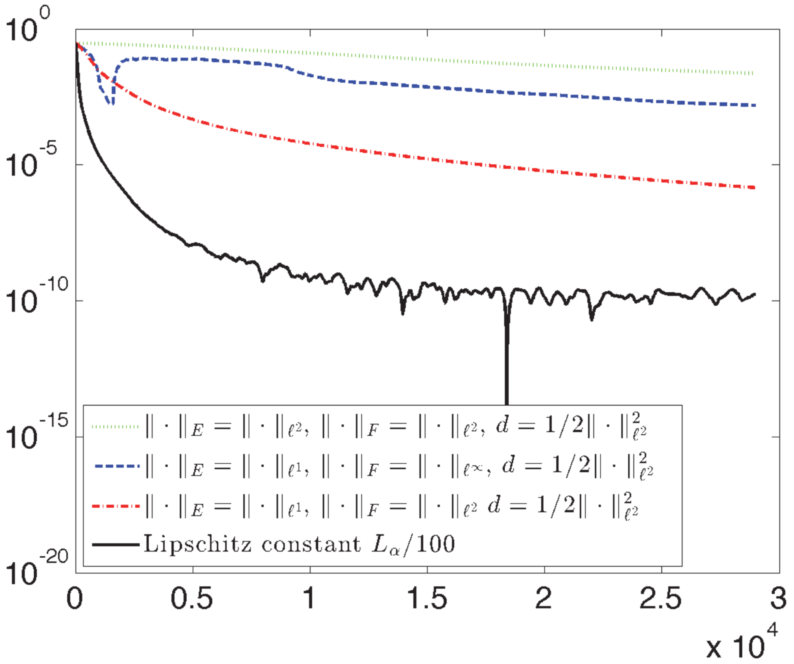

Figure 3. *Convergence curves in a semilogarithmic scale for Algorithm 1 ($\alpha = 10^{-2}$); number of iterations is on the x-axis. Green: the case where $\|.\|_E = \|.\|_{\ell^2}$, $\|.\|_F = \|.\|_{\ell^2}$, $d = \frac{1}{2}\|.\|_{\ell^2}^2$; red: the case where $\|.\|_E = \|.\|_{\ell^1}$, $\|.\|_F = \|.\|_{\ell^2}$, $d = \frac{1}{2}\|.\|_{\ell^2}^2$; blue: the case where $\|.\|_E = \|.\|_{\ell^1}$, $\|.\|_F = \|.\|_{\ell^\infty}$, $d = \frac{1}{2}\|.\|_{\ell^2}^2$; and black: the case where $\|.\|_E = \|.\|_{\ell^1}$, $\|.\|_F = \|.\|_{\ell^2}$, $d = \frac{1}{2}\|.\|_{\ell^2}^2$ with a restricted Lipschitz constant $L_\alpha^{'} = L_\alpha/100$.*

4.3. Numerical experiments on convergence.

In this section, we illustrate the improvement achieved by appropriately choosing the norms $\|.\|_E$, $\|.\|_F$, and the prox-function d. To do so, we run experiments on a dictionary of blocks of measurements all having the same size, $\ell = 256$, described in section 5.1, for 2D images of size 256×256. At first, we choose $\|.\|_E = \|.\|_{\ell^1}$, $\|.\|_F = \|.\|_{\ell^2}$, and $d = \frac{1}{2}\|.\|_{\ell^2}^2$, and we execute Algorithm 1 for this dictionary. In fact, this first case (where the norm on E differs from the usual $\|\cdot\|_{\ell^2}$) nearly corresponds to a standard accelerated gradient descent [NN04]. A second time, we set $\|.\|_E = \|.\|_{\ell^1}$, $\|.\|_F = \|.\|_{\ell^\infty}$, and $d = \frac{1}{2}\|.\|_{\ell^2}^2$. In Figure 3, we display the decrease of the objective function in both settings. The figure makes clear that a judicious selection of norms on E and F can significantly speed up the convergence: for 29,000 iterations, the standard accelerated projected gradient descent reaches a precision of 10^{-5}, whereas Algorithm 1 with $\|.\|_E = \|.\|_{\ell^1}$ and $\|.\|_F = \|.\|_{\ell^\infty}$—i.e., a "modified" gradient descent—reaches a precision of 10^{-3}. The conclusions for this numerical experiment appear to be faithful to what was predicted by the theory; see Proposition 4.5. For the sake of completeness, we add in Figure 3 (in green) the case where $\|.\|_E = \|.\|_{\ell^2}$, $\|.\|_F = \|.\|_{\ell^2}$, and $d = \frac{1}{2}\|.\|_{\ell^2}^2$, which is a usual choice in practice. Clearly, this is the slowest rate of convergence observed.

Finally, we execute the algorithm for $\|.\|_E = \|.\|_{\ell^1}$, $\|.\|_F = \|.\|_{\ell^2}$, and $d = \frac{1}{2}\|.\|_{\ell^2}^2$ by changing the value of L_α. The value of L_α provided by Proposition 4.3 is tight uniformly on B_∞. However, the local Lipschitz constant of ∇J_α varies rapidly inside the domain. In practice, the Lipschitz constant around the minimizer may be much smaller than L_α (note that $\pi^\star \in \mathrm{ri}(\Delta_m)$ for all $\alpha > 0$). In this last heuristic approach, we will decrease L_α by substantial factors without losing practical convergence. This result is presented in Figure 3, where the black curve denotes the convergence result when the Lipschitz constant L_α has been divided by 100. We can observe that in this case 1500 iterations suffice to reach the precision obtained by the case $\|.\|_E = \|.\|_{\ell^1}$, $\|.\|_F = \|.\|_{\ell^2}$, and $d = \frac{1}{2}\|.\|_{\ell^2}^2$ (in red) after 29,000 iterations. Let us give an intuitive explanation for this positive behavior. To simplify the reasoning, let us assume that $\boldsymbol{\pi}^\star$ is the uniform probability distribution. First notice that the choice of $\|\cdot\|_E$ influences only the Lipschitz constant of ∇J_α but does not change the algorithm, so we can play with the norm on E to decrease the local Lipschitz constant. Furthermore, the choice of $\|\cdot\|_E$ for minimizing the global Lipschitz constant may be different from that for minimizing the local Lipschitz constant. Considering that $\|\cdot\|_E = \|\cdot\|_{\ell^2}$, from (8) we get that $L_\alpha(\boldsymbol{q}^\star) = \frac{\|\boldsymbol{M}^*\|_{2\to 2}^2}{\alpha \sigma_{\mathcal{E}}(\boldsymbol{\pi}^\star)}$. Using the Perron–Frobenius theorem, it can be shown that $\|\boldsymbol{M}^*\|_{2\to 2}^2 = O(1)$ for our choice of dictionary, and $\sigma_{\mathcal{E}}(\boldsymbol{\pi}^\star) = m$ for $\|\cdot\|_E = \|\cdot\|_{\ell^2}$. From this simple reasoning, we can conclude that the local Lipschitz constant around $\boldsymbol{\pi}^\star$ is no greater than $O(1/m)$. This means that if the minimizer is sufficiently far away from the simplex boundary, we can decrease L_α by a significant factor without losing convergence.

5. Numerical results.

In this section, we assess the reconstruction performance of the sampling patterns using the approach described in section 4.2 with $\alpha = 10^{-2}$. We compare it to that of standard approaches used in the context of MRI. We call $\boldsymbol{\pi}[\boldsymbol{p}]$ the probability distribution $\boldsymbol{\pi}^\star$ resulting from the minimization problem (PP) for a given target distribution $\boldsymbol{p}$ on isolated measurements.

5.1. The choice of a particular dictionary of blocks.

From a numerical point of view, we study a particular system of blocks of measurements. The dictionary used in all numerical experiments in this article is composed of discrete lines of length ℓ, joining any pixel on the edge of the image to any pixel on the opposite edge, as in Figure 1(b). Note that the number of blocks in this dictionary is $n_1^2 + n_2^2$ for an image of size $n_1 \times n_2$. The choice of such a dictionary is particularly relevant in MRI, since the gradient waveforms that define the acquisition paths are subject to bounded-gradient and slew-rate constraints; see, e.g., [LKP08]. Moreover, the practical implementation on a scanner of straight lines is straightforward, since this approach is already in use in standard echo-planar imaging strategies.

Note that, in such a setting, the mapping $\boldsymbol{M}$, defined in (4), is a linear mapping that can be represented by a matrix of size $n \times m$ with $\boldsymbol{M}_{i,j} = 1/\ell$ when the ith pixel belongs to the jth block, for $i = 1, \dots, n$ and $j = 1, \dots, m$.

One may argue that in MRI, dealing with samples lying on continuous lines (and not discrete grids) is more realistic in the design of the magnetic resonance sequences. To deal with this issue, one could resort to the use of the nonuniform fast Fourier transform. That technique is, however, much more computationally intensive. In this paper we thus stick to values of the Fourier transform located on the Euclidean grid. This is commonly used in MRI with regridding techniques.

5.2. The reconstructed probability distribution.

We illustrate the fidelity of $\boldsymbol{\pi}[\boldsymbol{p}]$, the solution of problem (PP), to a given target $\boldsymbol{p}$. In the setting of 2D MR sensing, with the dictionary of lines in dimension $n_1 = n_2 = 256$ described in the previous subsection, we set the target probability distribution to $\boldsymbol{p} = \boldsymbol{p}_{\mathrm{opt}}$, the one suggested by current CS theories on the set of isolated measurements. This is proportional to $\|\boldsymbol{a}_k^*\|_{\ell^\infty}^2$; see [PVW11, CCW13, BBW13]. To give an idea of what the resulting probability distribution $\boldsymbol{\pi}[\boldsymbol{p}_{\mathrm{opt}}]$ looks like, we draw 100,000 independent blocks of measurements according to $\boldsymbol{\pi}[\boldsymbol{p}_{\mathrm{opt}}]$ and count the number of measurements for each discrete Fourier coefficient. The result is displayed in Figure 4. This experiment underlines that our strategy manages to catch the overall structure of the target probability distribution.

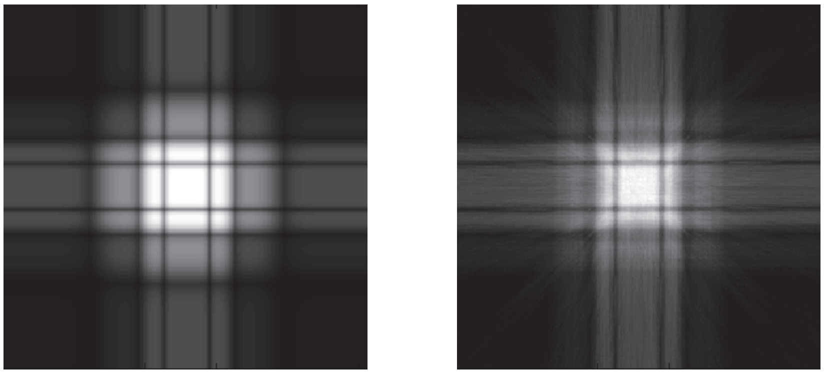
(a) (b)

Figure 4. *Illustration of the fidelity of* $\boldsymbol{\pi}[\boldsymbol{p}_{opt}]$ *to* $\boldsymbol{p}_{opt}$. (a) *The target probability distribution* $\boldsymbol{p}_{opt}$. (b) *The results of* 100,000 *i.i.d. drawings, performed according to* $\boldsymbol{\pi}[\boldsymbol{p}_{opt}]$, *of blocks from the blocks dictionary; we count the number of times that a point is sampled at each location. The gray level is proportional to the probability distribution* $\boldsymbol{p}$ *in* (a), *and to the number of points drawn on each location in* (b).

5.3. Reconstruction results.

In this section, we compare the reconstruction quality of MR images for different acquisition schemes. The comparison is always performed for schemes with an equivalent number of isolated measurements. We recall that in the case of MR images, the acquisition is done in the Fourier domain, and MR images are supposed to be sparse in the wavelet domain. Therefore, the full sensing matrix $\boldsymbol{A} = (\boldsymbol{a}_1|\boldsymbol{a}_2|\dots|\boldsymbol{a}_n)^*$, which models the acquisition process, is the composition of a Fourier transform with an inverse wavelet transform. The reconstruction is done via ℓ^1-minimization, as presented in (1), using the Douglas–Rachford algorithm [CP11b]. It was proven in various papers [CCW13, CCKW13, AHPR13] that MRI image quality can be greatly improved by fully acquiring the center of the Fourier domain via a mask defined by the support of the mother wavelet; see Figure 5. Therefore, for every type of scheme used in our reconstruction test, we first fully acquire this mask.

The various schemes considered in this paper are based on blocks of measurements and on heuristic schemes that are widely used in the context of MRI. They are described below.

- Equiangularly distributed radial lines: the scheme is made of lines always intersecting the center of the acquisition domain and distributed uniformly [LDSP08].
- Golden angle scheme: the scheme is made of radial lines separated by the golden angle, i.e., 111.246°. This technique is used often in MRI sequences, and it gives good

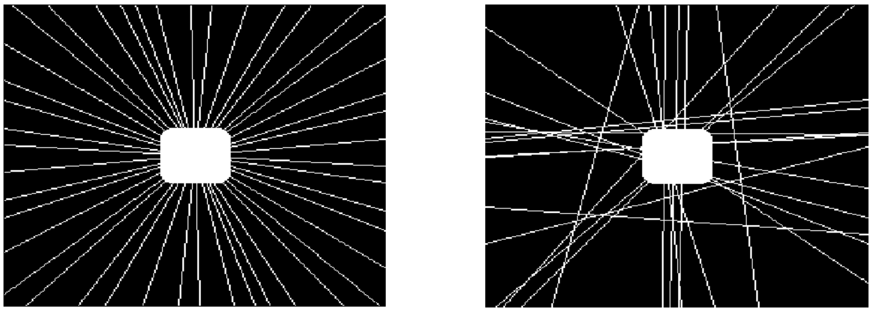

(a) (b)

Figure 5. *Different schemes based on* (a) *the golden angle pattern, and* (b) *the dictionary proposed in section* 5.1. *Both schemes are combined with a mask which fully samples the center of the Fourier domain. In both cases, the total measurements represent* 10% *of the full image, while the mask defined by the support of the mother wavelet represents* 3% *of the full image.*

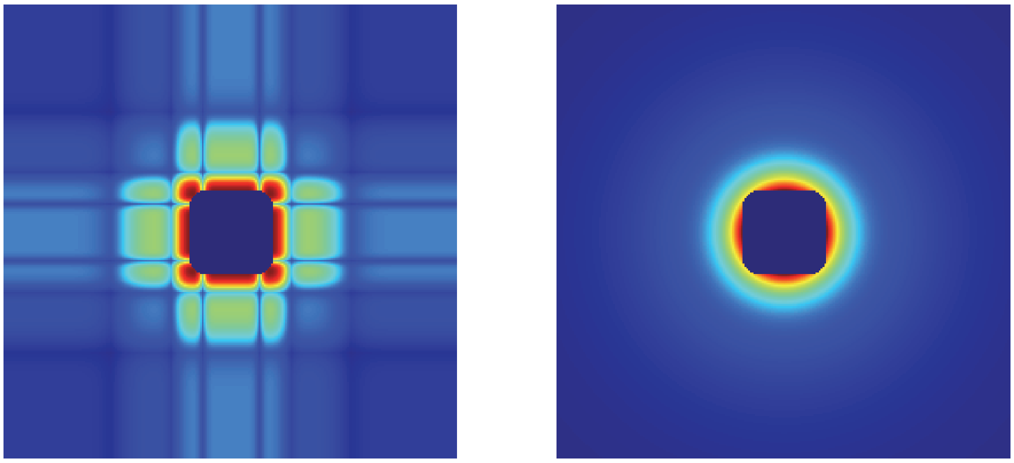

(a) (b)

Figure 6. *Target probabilities on pixels: in red, high values, and in dark blue, values close to* 0. (a) *The distribution proportional to* $\|\boldsymbol{a}_i^*\|_{\ell^\infty}^2$ *defined in* [CCW13]. (b) *A radial distribution, as presented in* [KW12]. *The center has been set to zero, since it will be sampled by the mask in a deterministic way.*

reconstruction results in practice [WSK$^+$07].

- Random radial scheme: radial lines are drawn uniformly at random [CRCP12].
- Scheme based on the dictionary described in section 5.1:
  - Blocks are drawn according to $\boldsymbol{\pi}\,[\boldsymbol{p}_{\text{rad}}]$, which is the probability distribution obtained by minimizing problem (PP) for $\boldsymbol{p} = \boldsymbol{p}_{\text{rad}}$. The distribution $\boldsymbol{p}_{\text{rad}}$ is a radial distribution that decreases as $\mathcal{O}\big(\frac{1}{k_x^2+k_y^2}\big)$. This choice was justified recently in [KW12] and used extensively in practice. Note that $\boldsymbol{p}_{\text{rad}}$ is set to 0 on the k-space center since it is already sampled deterministically; see Figure 6(b).
  - Blocks are drawn according to $\boldsymbol{\pi}\,[\boldsymbol{p}_{\text{opt}}]$, where $\boldsymbol{p}_{\text{opt}}$ is defined by (3), which is the probability distribution obtained by minimizing problem (PP) for $\boldsymbol{p} = \boldsymbol{p}_{\text{opt}}$ defined in [CCW13, BBW13]. Once again, $\boldsymbol{p}_{\text{opt}}$ is set to 0 on the k-space center; see Figure 6(a).

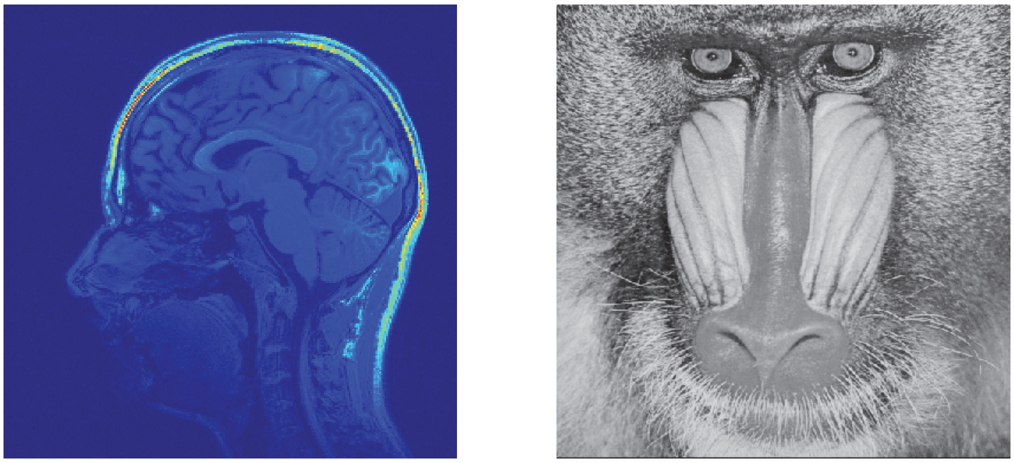

(a) Brain. (b) Baboon.

Figure 7. *Reference images to be reconstructed for the settings* 256×256 *and* 512×512.

Setting 256×256. The numerical experiment is run for images of size $n_0 \times n_0$ with $n_0 = 256$. The full dictionary described in section 5.1 contains lines of length $\ell = n_0$ pixels connecting every point on the edge of the image to every point on the opposite side. For each proportion of measurements $(10\%, 15\%, 20\%, 25\%, 30\%, 40\%, 50\%)$ we proceed to 100 drawings of schemes when the considered scheme is random. Reconstruction results, for the reference images shown in Figure 7 and for various sampling schemes, are displayed in terms of means of peak signal-to-noise ratio (PSNR) in Figure 8(a) and (c).

Figure 8 shows that the schemes based on the approach presented in this article give better results than do random radial schemes, for any proportion of measurements. The improvement in terms of PSNR is generally between 1 and 2 dB. The schemes based on $\boldsymbol{\pi}[\boldsymbol{p}_{\mathrm{opt}}]$ and $\boldsymbol{\pi}[\boldsymbol{p}_{\mathrm{rad}}]$ are competitive with those based on the golden angle or equiangularly distributed schemes in the case where the proportion of measurements is low (less than 20% of measurements). We observe that for 10% measurements, schemes based on our dictionary and drawn according to $\boldsymbol{\pi}[\boldsymbol{p}_{\mathrm{rad}}]$ outperform the standard sampling strategies by more than 1 dB. Increasing the PSNR by 1 dB is significant and can be qualitatively observed in the reconstructed image.

In Figures 8(a) and (c), it can be seen that block-constrained acquisition never outperforms acquisitions based on independent measurements. This was to be expected since adding constraints reduces the space of possible sampling patterns. Once again, note that independent drawings are, however, not conceivable in many contexts such as MRI. In a nutshell, we can say that the proposed sampling approach always produces results comparable to those of the standard sampling schemes and tends to produce better results for low sampling ratios.

Finally, in Figure 9, we illustrate that block-constrained acquisition does not allow us to reach an arbitrary target distribution by showing the difference between $\boldsymbol{p}_{\mathrm{rad}}$ and the probability distribution $\boldsymbol{M}(\boldsymbol{\pi}[\boldsymbol{p}_{\mathrm{rad}}])$, which is defined on the set of isolated measurements. This confirms Proposition 3.2 experimentally.

Setting 512×512. Given that in CS the quality of the reconstruction can be resolution dependent, as described in [AHPR13], we decided to run the same numerical experiment on

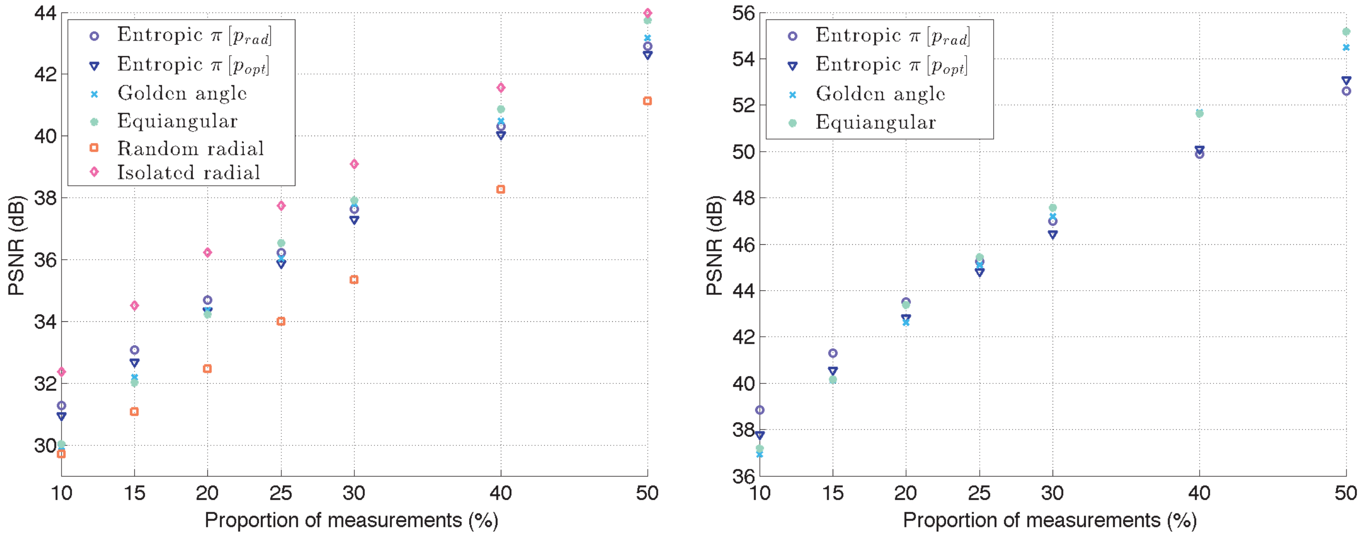

(a) Brain in 256 × 256. (b) Brain in 512 × 512.

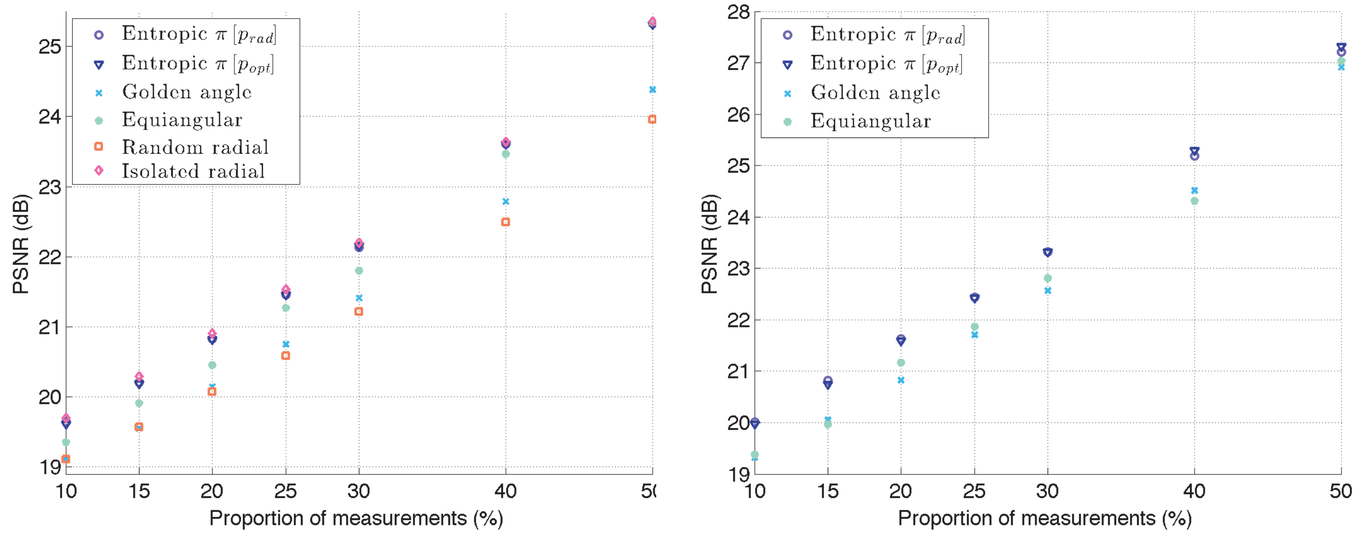

(c) Baboon in 256 × 256. (d) Baboon in 512 × 512.

Figure 8. *PSNR means of the reconstructed images (brain, baboon) w.r.t. the proportion of measurements chosen in the scheme* $(10\%, 15\%, 20\%, 25\%, 30\%, 40\%, 50\%)$*. The undersampling ratio for all schemes is the ratio between the number of sampled distinct frequencies and the total number of possible measurements. This means that duplicated frequencies are accounted for only once.*

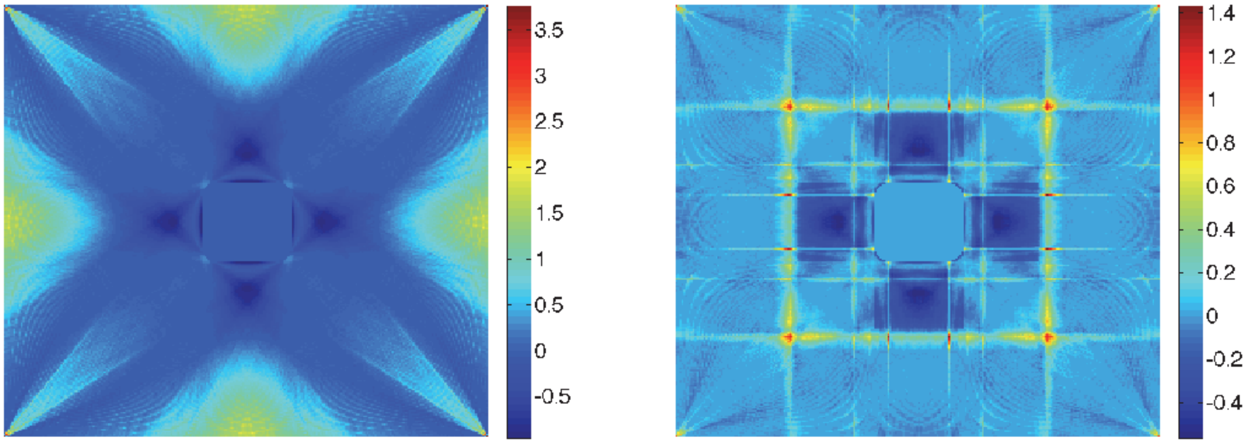

(a) (b)

Figure 9. *Difference between the target probabilities* $\boldsymbol{p}$ *and* $\boldsymbol{M}\boldsymbol{\pi}(\boldsymbol{p})$ *relative to the magnitude of* $\boldsymbol{p}$*; i.e., we show the quantity* $\frac{(\boldsymbol{M}(\boldsymbol{\pi}(\boldsymbol{p})))_i - \boldsymbol{p}_i}{\boldsymbol{p}_i}$ *for the ith sampling location.* (a) *For the radial distribution* $\boldsymbol{p}_{rad}$*, we see that we "subdraw" by a factor of* 50% *around the mask, and we "overdraw" by a factor of* $150\%S$ *at the center of the edges.* (b) *For the CS optimal distribution* $\boldsymbol{p}_{opt}$*, we see that we "subdraw" by a factor of* 40% *around the mask. Note that the subdrawing effect cannot be avoided: indeed, we cannot reach any target probability distribution via* $\boldsymbol{M}$*; see Proposition* 3.2*.*

512×512 images. The numerical experiment was run for images of size $n_0 \times n_0$ with $n_0 = 512$. The full dictionary described in section 5.1 contains lines of length $\ell = n_0$ connecting every point on the edge of the image to every point on the opposite side. For each proportion of measurements $(10\%, 15\%, 20\%, 25\%, 30\%, 40\%, 50\%)$, and for each random sampling scheme, we test image reconstruction from 10 drawn sampling schemes. The reference images to be reconstructed are the same as were used in the setting 256×256; see Figure 7.

Quality of reconstructions is compared in Figure 8(b) and (d) for the golden or equiangularly distributed lines and our proposed method based on $\boldsymbol{\pi}(\boldsymbol{p}_{\text{opt}})$ and $\boldsymbol{\pi}(\boldsymbol{p}_{\text{rad}})$. This experiment shows that the PSNR of the reconstructed images is significantly improved by using the proposed method, until 30% of measurements for the brain image and 40% of measurements for the baboon image. We can remark that for both images, for the same proportion of measurements, the PSNR of the reconstructed images increases as the resolution increases. This numerical experiment suggests that the proposed sampling approach might be significantly better than traditional ones in the MRI context for high resolution images. In Figure 10(a), we present the brain image reconstructed from 15% of measurements in the case of a golden angle scheme. In Figure 10(b), we present the brain image reconstructed from 15% of measurements in the case of a realization of a scheme based on $\boldsymbol{\pi}(\boldsymbol{p}_{\text{rad}})$. The latter's PSNR is 41.88 dB, whereas in the golden scheme case, the PSNR reaches only 40.13 dB. In Figure 10(c) and (d), we display the corresponding difference images relative to the reference image, which underlines the improvement of 1.7 dB in our method.

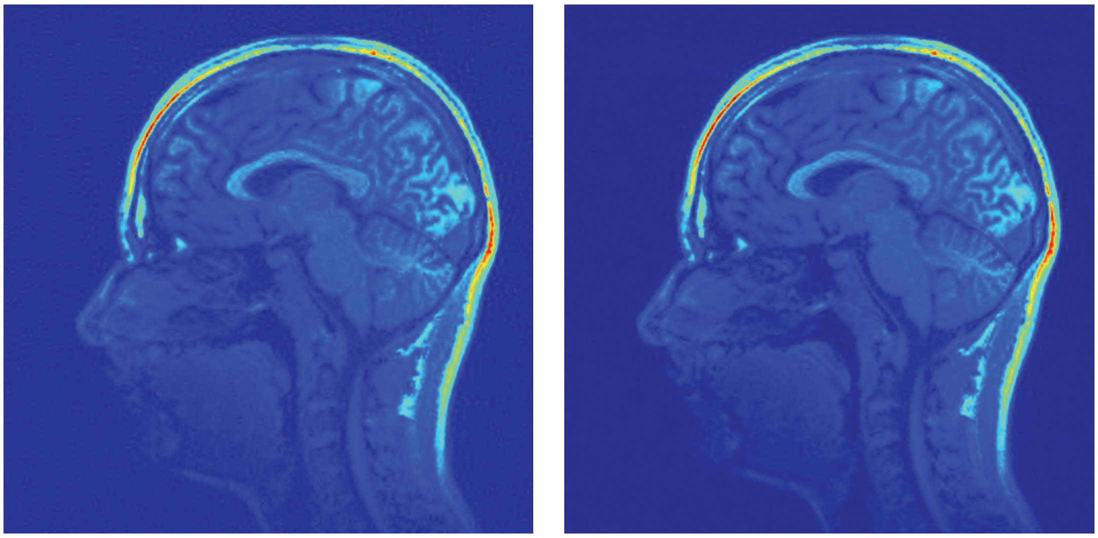

(a) PSNR = 40.1364 dB. (b) PSNR = 41.8854 dB.

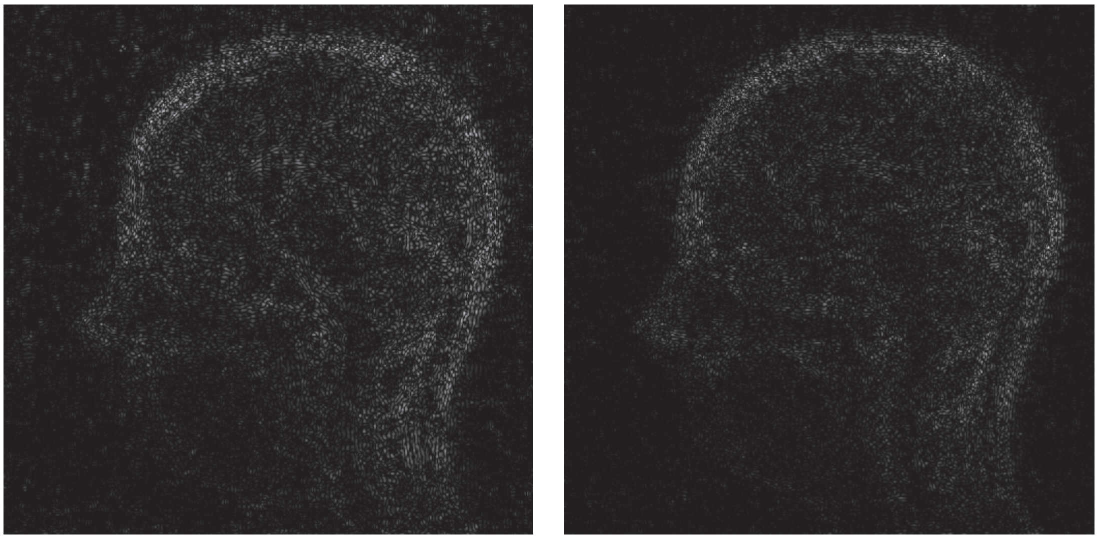

(c) (d)

Figure 10. *Comparison of the reconstructed images from* 15% *of measurements for a* 512×512 *image for a golden angle scheme* (a) *and a scheme based on our dictionary and* $\boldsymbol{\pi}(\boldsymbol{p}_{rad})$ (b)*. We plot the absolute difference between the reference and the reconstructed image for the reconstruction using a golden angle scheme* (c) *or a scheme based on* $\boldsymbol{\pi}(\boldsymbol{p}_{rad})$ (d)*. Note that in* (c) *and* (d)*, the gray levels are in the same scale.*

As a side note, let us mention that in MRI, sampling diagonal or horizontal lines actually takes the same scanning time (even though the diagonals are longer), since gradient coils work independently in each direction. In the MRI example, the length of the path is thus less meaningful than the number of scanned lines. In Figure 11, we show different sampling schemes based on the golden angle pattern or on our method with the same number of lines, and we show the corresponding reconstructions of brain images.

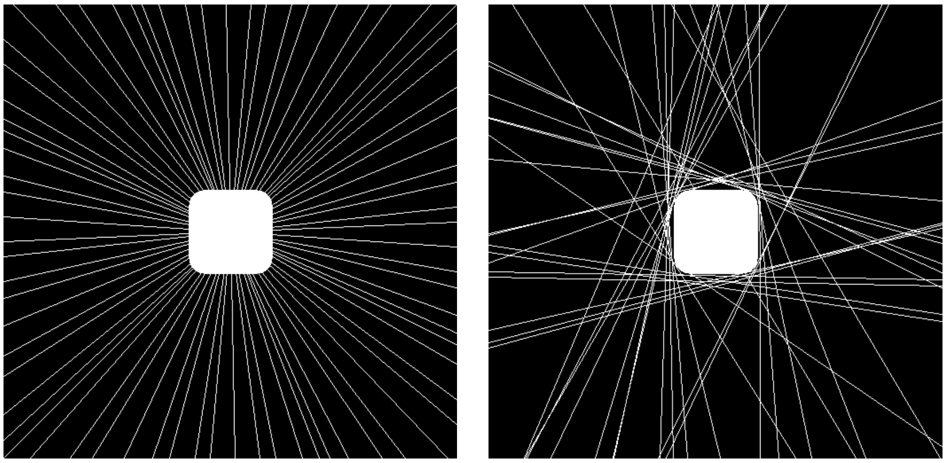

(a) Golden angle scheme (9.2%). (b) $\pi(p_{\mathrm{rad}})$-based scheme (10%).

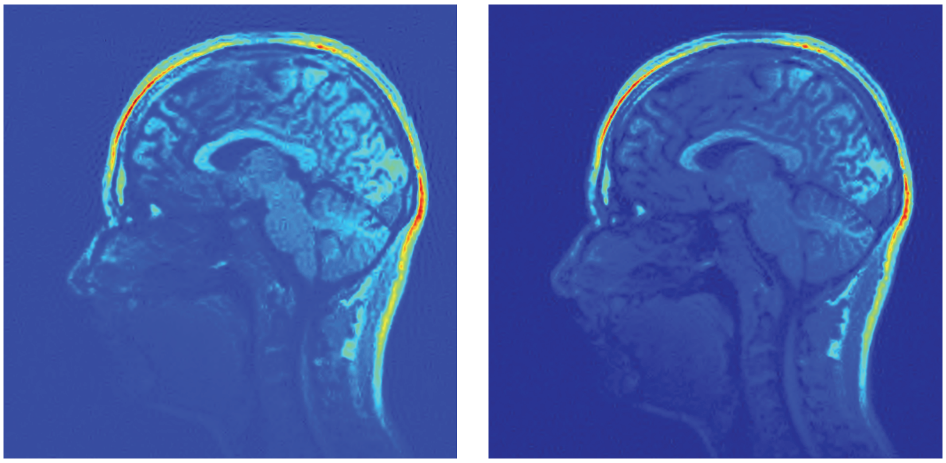

(c) PSNR = 36.34 dB. (d) PSNR = 38.99 dB.

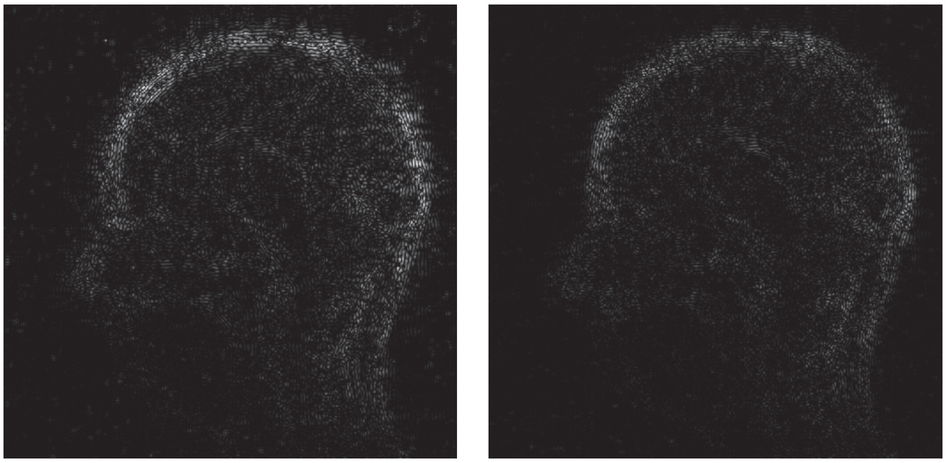

(e) Golden angle. (f) $\boldsymbol{\pi}(\boldsymbol{p}_{\mathrm{rad}})$-based scheme.

Figure 11. *Reconstruction examples. We plot schemes made of* 37 *lines based on the golden angle pattern* (a) *or our method with* $\boldsymbol{\pi}(\boldsymbol{p}_{rad})$ (b)*. Drawing* 37 *lines in both cases leads to a cover of the sampling space by* 9.2% *in the case of the golden angle scheme, and by* 10% *for the* $\boldsymbol{\pi}(\boldsymbol{p}_{rad})$*-based scheme. Note that, despite a difference of* 0.8% *in the covering of the* k*-space, the scanning time is the same for both schemes. In* (c) *and* (d) *we display the corresponding reconstructions via* ℓ^1*-minimization. We can see that we improve the reconstruction by more than 2 dB with our method. At the bottom, we show the corresponding absolute difference with the reference image. Note that the gray levels have the same scaling in* (e) *and* (f)*.*

Remark. In both settings, for the brain image, schemes based on $\boldsymbol{\pi}\,[\boldsymbol{p}_{\text{rad}}]$ lead to better reconstruction results in terms of PSNR than do schemes from $\boldsymbol{\pi}\,[\boldsymbol{p}_{\text{opt}}]$. This can be explained by the fact that $\boldsymbol{p}_{\text{opt}}$ is the probability density given by CS theory, which provides guarantees to reconstruct any s-sparse signal. However, brain images or natural images have a structured sparsity in the wavelet domain: indeed, their wavelet transform is not uniformly s-sparse; the approximation part contains more nonzero coefficients than do the rest of the detailed parts. We can infer that $\boldsymbol{p}_{\text{rad}}$ manages to catch the sparsity structure of the wavelet coefficients of the considered images.

6. Conclusion.

In this paper, we have focused on constrained acquisition by blocks of measurements. Sampling schemes are constructed by drawing blocks of measurements from a given dictionary of blocks according to a probability distribution $\boldsymbol{\pi}$ that needs to be chosen in an appropriate way. We have presented a novel approach to computing $\boldsymbol{\pi}$ in order to imitate existing sampling schemes in CS that are based on the drawing of isolated measurements. For this purpose, we have defined a notion of the dissimilarity measure between a probability distribution on a dictionary of blocks and a probability distribution on a set of isolated measurements. This setting leads to a convex minimization problem in high dimension. In order to compute a solution to this optimization problem, we proposed an efficient numerical approach based on the work of [Nes05]. Our numerical study highlights the fact that performing minimization on a metric space rather than a Hilbert space might lead to significant acceleration. Finally, we have presented reconstruction results using this new approach in the case of MRI acquisition. Our method seems to provide better reconstruction results than do standard strategies used in this domain. We believe that this last point brings interesting perspectives for 3D MRI reconstruction.

In future work, we plan to extend the proposed numerical method to a wider setting and to provide better theoretical guarantees for cases where the Lipschitz constant of the gradient may vary across the domain. A first step in this direction was proposed recently in [GK13]. We also plan to accelerate the matrix-vector product involving $\boldsymbol{M}$ by using fast Radon transforms. This step is unavoidable in applying our algorithm to 3D or 3D+t problems, for which we expect important benefits compared to the small images we have tested thus far. Finally, we are currently collaborating with physicists at Neurospin, CEA and plan to implement the proposed sampling schemes on real MRI scanners.

Appendix A. Proof of Proposition 4.1.

First, we express the Fenchel–Rockafellar dual problem [Roc97]:

$$\begin{aligned}
&\min_{\boldsymbol{\pi}\in\Delta_m} \|\boldsymbol{p}-\boldsymbol{M}\boldsymbol{\pi}\|_{\ell^1} + \alpha\mathcal{E}(\boldsymbol{\pi})\\
&\qquad = \min_{\boldsymbol{\pi}\in\Delta_m}\max_{\boldsymbol{q}\in B_\infty} \langle \boldsymbol{M}\boldsymbol{\pi}-\boldsymbol{p},\boldsymbol{q}\rangle_{F^*\times F} + \alpha\mathcal{E}(\boldsymbol{\pi})\\
&\qquad = \max_{\boldsymbol{q}\in B_\infty}\min_{\boldsymbol{\pi}\in\Delta_m} \langle \boldsymbol{M}^*\boldsymbol{q},\boldsymbol{\pi}\rangle_{E^*\times E} - \langle \boldsymbol{p},\boldsymbol{q}\rangle_{F^*\times F} + \alpha\mathcal{E}(\boldsymbol{\pi})\\
&\qquad = \max_{\boldsymbol{q}\in B_\infty} -J_\alpha(\boldsymbol{q}),
\end{aligned}$$

where B_∞ stands for the ℓ^∞-ball of unit radius and

$$J_\alpha(\boldsymbol{q}) = -\min_{\boldsymbol{\pi}\in\Delta_m} \langle \boldsymbol{M}^*\boldsymbol{q},\boldsymbol{\pi}\rangle_{E^*\times E} - \langle \boldsymbol{p},\boldsymbol{q}\rangle_{F^*\times F} + \alpha\mathcal{E}(\boldsymbol{\pi}). \tag{16}$$

The solution $\boldsymbol{\pi}(\boldsymbol{q})$ of the minimization problem (16) satisfies

$$\boldsymbol{M}^*\boldsymbol{q} + \alpha\left(\log(\boldsymbol{\pi}(\boldsymbol{q})) + 1\right) \in -\mathcal{N}_{\Delta_m}(\boldsymbol{\pi}(\boldsymbol{q})) \quad \text{if } \boldsymbol{\pi}(\boldsymbol{q}) \in \mathrm{ri}\left(\Delta_m\right), \tag{17}$$

where $\mathcal{N}_{\Delta_m}(\boldsymbol{\pi}(\boldsymbol{q}))$ denotes the normal cone to the set Δ_m at the point $\boldsymbol{\pi}(\boldsymbol{q})$, and $\mathrm{ri}\left(\Delta_m\right)$ denotes the relative interior of Δ_m. Equation (17) can be rewritten in the following way:

$$\boldsymbol{M}^*\boldsymbol{q} + \alpha \log(\boldsymbol{\pi}(\boldsymbol{q})) = (-\lambda - \alpha)\mathbb{1}, \qquad \text{with } \lambda \in \mathbb{R}^+ \text{ and } \boldsymbol{\pi}(\boldsymbol{q}) \in \Delta_m. \tag{18}$$

By choosing $\lambda = \alpha \log\left(\sum_{k=1}^m \exp\left(-\frac{(\boldsymbol{M}^*\boldsymbol{q})_k}{\alpha}\right)\right) - \alpha$ and plugging this into (18), we get that

$$(\boldsymbol{\pi}(\boldsymbol{q}))_j = \frac{\exp\left(-\frac{(\boldsymbol{M}^*\boldsymbol{q})_j}{\alpha}\right)}{\sum_{k=1}^m \exp\left(-\frac{(\boldsymbol{M}^*\boldsymbol{q})_k}{\alpha}\right)} \qquad \forall j \in \{1,\dots,m\}. \tag{19}$$

It remains to plug (19) into (16) to obtain (DP) with

$$J_\alpha(\boldsymbol{q}) = \langle \boldsymbol{p}, \boldsymbol{q}\rangle_{F^*\times F} - \alpha \log\left(\sum_{k=1}^m \exp\left(-\frac{(\boldsymbol{M}^*\boldsymbol{q})_k}{\alpha}\right)\right).$$

Appendix B. Proof of Proposition 4.2. The neg-entropy is continuous and twice continuously differentiable on $\mathrm{ri}\left(\Delta_m\right)$. Then, in order to prove its strong convexity, it is sufficient to bound from below its positive diagonal Hessian w.r.t. $\|\cdot\|_E$. We have

$$\left\langle \mathcal{E}''(\boldsymbol{\pi})\boldsymbol{h}, \boldsymbol{h}\right\rangle = \sum_{i=1}^m \frac{(h_i)^2}{\pi_i} \qquad \text{for } \boldsymbol{\pi} \in \mathrm{ri}\left(\Delta_m\right) \text{ and } \boldsymbol{h} \in \mathbb{R}^m. \tag{20}$$

Using the Cauchy–Schwarz inequality,

$$\begin{aligned}\|\boldsymbol{h}\|_{\ell^1}^2 = \left(\sum_{i=1}^m \frac{|h_i|}{\sqrt{\pi_i}}\sqrt{\pi_i}\right)^2 &\le \left(\sum_{i=1}^m \frac{h_i^2}{\pi_i}\right)\left(\sum_{i=1}^m \pi_i\right) \\ &\le \underbrace{\|\boldsymbol{\pi}\|_{\ell^1}}_{=1}\left\langle \mathcal{E}''(\boldsymbol{\pi})\boldsymbol{h}, \boldsymbol{h}\right\rangle.\end{aligned}$$

Therefore, $\mathcal{E}$ is 1-strongly convex on the simplex w.r.t. $\|.\|_{\ell^1}$. Since for all $p \in [1,\infty]$, $\|.\|_{\ell^1} \ge \|.\|_p$, we get

$$\|\boldsymbol{h}\|_{\ell^p}^2 \le \left\langle \mathcal{E}''(\boldsymbol{\pi})\boldsymbol{h}, \boldsymbol{h}\right\rangle \quad \forall \boldsymbol{h} \in \mathbb{R}^m,\ \boldsymbol{\pi} \in \mathrm{ri}\left(\Delta_m\right).$$

Moreover, if $(\boldsymbol{\pi}_n)_{n\in\mathbb{N}}$ denotes a sequence of $\mathrm{ri}(\Delta_m)$ pointwise converging to the first element of the canonical basis e_1 and $h = e_1$, then

$$\lim_{n\to+\infty} \langle \mathcal{E}''(\boldsymbol{\pi}_n)h, h\rangle = \|h\|_{\ell^p}^2 = 1,$$

so that the inequality is tight.

Appendix C. Proof of Proposition 4.3. The proof is based on arguments similar to those of [Nes05, Theorem 1]. First, notice that

$$
\begin{aligned}
&\left\langle \nabla\mathcal{E}\left(\boldsymbol{\pi}(\boldsymbol{q}_2)\right) - \nabla\mathcal{E}\left(\boldsymbol{\pi}(\boldsymbol{q}_1)\right), \boldsymbol{\pi}(\boldsymbol{q}_2) - \boldsymbol{\pi}(\boldsymbol{q}_1)\right\rangle \\
&\quad = \left\langle \int_{t=0}^{1} \mathcal{E}''(\boldsymbol{\pi}_1 + t(\boldsymbol{\pi}_2 - \boldsymbol{\pi}_1))(\boldsymbol{\pi}_2 - \boldsymbol{\pi}_1)dt, \boldsymbol{\pi}(\boldsymbol{q}_2) - \boldsymbol{\pi}(\boldsymbol{q}_1) \right\rangle \\
&\quad \geq \sigma_{\mathcal{E}}\left[\boldsymbol{\pi}_1, \boldsymbol{\pi}_2\right] \|\boldsymbol{\pi}_2 - \boldsymbol{\pi}_1\|_E^2, \qquad (21)
\end{aligned}
$$

where

$$\sigma_{\mathcal{E}}\left[\boldsymbol{\pi}_1, \boldsymbol{\pi}_2\right] = \inf_{t\in[0,1]} \sigma_{\mathcal{E}}(t\boldsymbol{\pi}_1 + (1-t)\boldsymbol{\pi}_2)$$

is the local convexity modulus of $\mathcal{E}$ on the segment $[\boldsymbol{\pi}(\boldsymbol{q}_1), \boldsymbol{\pi}(\boldsymbol{q}_2)]$.

Next, recall that

$$J_\alpha(\boldsymbol{q}) = \max_{\boldsymbol{\pi}\in\Delta_m} \langle -\boldsymbol{M}^*\boldsymbol{q}, \boldsymbol{\pi}\rangle_{E^*\times E} + \langle \boldsymbol{p}, \boldsymbol{q}\rangle_{F^*\times F} - \alpha\mathcal{E}(\boldsymbol{\pi}).$$

The optimality conditions of the previous maximization problem for $J_\alpha(\boldsymbol{q}_1)$ and $J_\alpha(\boldsymbol{q}_1)$, $\boldsymbol{q}_1, \boldsymbol{q}_2 \in F$, lead to

$$
\begin{aligned}
\left\langle -\boldsymbol{M}^*\boldsymbol{q}_1 - \alpha\nabla\mathcal{E}\left(\boldsymbol{\pi}(\boldsymbol{q}_1)\right), \boldsymbol{\pi}(\boldsymbol{q}_2) - \boldsymbol{\pi}(\boldsymbol{q}_1)\right\rangle \leq 0, \\
\left\langle -\boldsymbol{M}^*\boldsymbol{q}_2 - \alpha\nabla\mathcal{E}\left(\boldsymbol{\pi}(\boldsymbol{q}_2)\right), \boldsymbol{\pi}(\boldsymbol{q}_1) - \boldsymbol{\pi}(\boldsymbol{q}_2)\right\rangle \leq 0.
\end{aligned}
$$

Combining the two previous inequalities, we can write that for $\boldsymbol{q}_1, \boldsymbol{q}_2 \in F$

$$
\begin{aligned}
&\langle \boldsymbol{M}^*(\boldsymbol{q}_1 - \boldsymbol{q}_2), \boldsymbol{\pi}(\boldsymbol{q}_1) - \boldsymbol{\pi}(\boldsymbol{q}_2)\rangle \geq \alpha \left\langle \nabla\mathcal{E}\left(\boldsymbol{\pi}(\boldsymbol{q}_2)\right) - \nabla\mathcal{E}\left(\boldsymbol{\pi}(\boldsymbol{q}_1)\right), \boldsymbol{\pi}(\boldsymbol{q}_2) - \boldsymbol{\pi}(\boldsymbol{q}_1)\right\rangle \\
&\Longrightarrow \|\boldsymbol{M}^*(\boldsymbol{q}_1 - \boldsymbol{q}_2)\|_{E^*} \|\boldsymbol{\pi}(\boldsymbol{q}_1) - \boldsymbol{\pi}(\boldsymbol{q}_2)\|_E \overset{(21)}{\geq} \alpha\sigma_{\mathcal{E}}\left[\boldsymbol{\pi}(\boldsymbol{q}_1), \boldsymbol{\pi}(\boldsymbol{q}_2)\right] \|\boldsymbol{\pi}(\boldsymbol{q}_1) - \boldsymbol{\pi}(\boldsymbol{q}_2)\|_E^2 \\
&\Longrightarrow \|\boldsymbol{M}^*\|_{F\to E^*} \|\boldsymbol{q}_1 - \boldsymbol{q}_2\|_F \|\boldsymbol{\pi}(\boldsymbol{q}_1) - \boldsymbol{\pi}(\boldsymbol{q}_2)\|_E \geq \alpha\sigma_{\mathcal{E}}\left[\boldsymbol{\pi}(\boldsymbol{q}_1), \boldsymbol{\pi}(\boldsymbol{q}_2)\right] \|\boldsymbol{\pi}(\boldsymbol{q}_1) - \boldsymbol{\pi}(\boldsymbol{q}_2)\|_E^2.
\end{aligned}
$$

Therefore, we can write that

$$\|\boldsymbol{\pi}(\boldsymbol{q}_1) - \boldsymbol{\pi}(\boldsymbol{q}_2)\|_E \leq \frac{\|\boldsymbol{M}^*\|_{F\to E^*} \|\boldsymbol{q}_1 - \boldsymbol{q}_2\|_F}{\alpha\sigma_{\mathcal{E}}\left[\boldsymbol{\pi}(\boldsymbol{q}_1), \boldsymbol{\pi}(\boldsymbol{q}_2)\right]}.$$

Noting that $\nabla J_\alpha(\boldsymbol{q}) = -\boldsymbol{M}\boldsymbol{\pi}(\boldsymbol{q}) + \boldsymbol{p}$, we can conclude that

$$
\begin{aligned}
\|\nabla J_\alpha(\boldsymbol{q}_1) - \nabla J_\alpha(\boldsymbol{q}_2)\|_{F^*} &= \|\boldsymbol{M}\left(\boldsymbol{\pi}(\boldsymbol{q}_1) - \boldsymbol{\pi}(\boldsymbol{q}_2)\right)\|_{F^*} \\
&\leq \|\boldsymbol{M}^*\|_{F\to E^*} \|\boldsymbol{\pi}(\boldsymbol{q}_1) - \boldsymbol{\pi}(\boldsymbol{q}_2)\|_E \\
&\leq \frac{\|\boldsymbol{M}^*\|_{F\to E^*}^2}{\alpha\sigma_{\mathcal{E}}\left[\boldsymbol{\pi}(\boldsymbol{q}_1), \boldsymbol{\pi}(\boldsymbol{q}_2)\right]} \|\boldsymbol{q}_1 - \boldsymbol{q}_2\|_F.
\end{aligned}
$$

Let us consider a sequence $(\boldsymbol{q}_n)_{n\in\mathbb{N}}$ converging uniformly towards $\boldsymbol{q} \in B_\infty \subset F$. Since $\boldsymbol{\pi} : \boldsymbol{q} \in B_\infty \longmapsto \boldsymbol{\pi}(\boldsymbol{q}) \in \Delta_m$ is a continuous mapping, $\boldsymbol{\pi}_n := \boldsymbol{\pi}(\boldsymbol{q}_n)$ converges uniformly towards $\boldsymbol{\pi}(\boldsymbol{q})$. Thus,

$$\sigma_{\mathcal{E}}\left[\boldsymbol{\pi}(\boldsymbol{q}_n), \boldsymbol{\pi}(\boldsymbol{q})\right] \underset{n\to+\infty}{\longrightarrow} \sigma_{\mathcal{E}}(\boldsymbol{\pi}(\boldsymbol{q})).$$

Appendix D. Proof of Theorem 4.6. Theorem 4.6 is a direct consequence of Lemma D.1 below. A similar proof was proposed in [FP11] but not extended to a general setting.

Lemma D.1. *Let $f : \mathbb{R}^m \to \mathbb{R} \cup \{+\infty\}$ and $g : \mathbb{R}^n \to \mathbb{R} \cup \{+\infty\}$ denote closed convex functions such that $A \cdot ri(dom(f)) \cap ri(dom(g)) \neq \emptyset$. Assume further that g is σ-strongly convex w.r.t. an arbitrary norm $\|\cdot\|$. Then we have the following:*

(i) *Function* g^* *satisfies* $\mathrm{dom}(g^*) = \mathbb{R}^n$ *and is differentiable on* $\mathbb{R}^n$.

(ii) *Define*

$$p(x) = f(Ax) + g(x), \tag{22}$$

$$d(y) = -g^*(-A^*y) - f^*(y), \tag{23}$$

and

$$x(y) = \nabla g^*(-A^*y).$$

Let x^* *denote the minimizer of* (22) *and* y^* *denote any minimizer of* (23). *Then for any* $y \in \mathbb{R}^m$ *we have*

$$\|x(y) - x^*\|^2 \leq \frac{2}{\sigma}\left(d(y) - d(y^*)\right). \tag{24}$$

Proof. Point (i) is a standard result in convex analysis. See, e.g., [HUL96]. We did not find the result (ii) in standard textbooks, and to our knowledge it is new. We assume for simplicity that g, g^*, f, and f^* are differentiable. This hypothesis is not necessary and can be avoided at the expense of longer proofs. First note that

$$\inf_{x\in\mathbb{R}^n} p(x) = \sup_{y\in\mathbb{R}^m} -g^*(-A^*y) - f^*(y),$$

by the Fenchel–Rockafellar duality. Since g is strongly convex, ∇g is a one-to-one mapping and

$$\nabla g(\nabla g^*(x)) = x \quad \forall x \in \mathbb{R}^n. \tag{25}$$

The primal-dual relationships read

$$\begin{cases} A^*y^* + \nabla g(x^*) &= 0, \\ Ax^* - \nabla f^*(y^*) &= 0, \end{cases}$$

so that

$$\begin{aligned} x^* &= (\nabla g)^{-1}(-A^*y^*) \\ &= (\nabla g^*)(-A^*y^*). \end{aligned}$$

Let us define the following Bregman divergence quantities:

$$\begin{aligned} D_1(y) &:= f^*(y) - f^*(y^*) - \langle A\nabla g^*(-A^*y^*), y - y^*\rangle, \\ D_2(y) &:= g^*(-A^*y) - g^*(-A^*y^*) + \langle A\nabla g^*(-A^*y^*), y - y^*\rangle. \end{aligned}$$

By construction,

$$D_1(y) + D_2(y) = d(y) - d(y^*).$$

Moreover, since y^* is the minimizer of d, it satisfies $A\nabla g^*(-A^*y^*) = \nabla f^*(y^*)$. By replacing this expression in D_1 and using the fact that f^* is convex, we get that

$$D_1(y) \geq 0 \quad \forall y \in \mathbb{R}^n.$$

Using identity (25), we get

$$D_2(y) = g^*(\nabla g(x(y))) - g^*(\nabla g(x^*)) + \langle x^*, \nabla g(x^*) - \nabla g(x(y))\rangle. \tag{26}$$

Moreover, since (see, e.g., [HUL96])

$$g(x) + g^*(x^*) = \langle x, x^*\rangle \Leftrightarrow x^* = \nabla g(x),$$

we get that

$$g^*(\nabla g(x(y))) = \langle \nabla g(x(y)), x(y)\rangle - g(x(y))$$

and

$$g^*(\nabla g(x^*)) = \langle \nabla g(x^*), x^*\rangle - g(x^*).$$

Replacing these expressions in (26), we obtain

$$\begin{aligned} D_2(y) &= g(x^*) - g(x(y)) + \langle \nabla g(x(y)), x(y) - x^*\rangle \\ &\geq \frac{\sigma}{2}\|x(y) - x^*\|^2, \end{aligned}$$

since g is σ strongly convex w.r.t. $\|\cdot\|$. To sum up, we have

$$\begin{aligned} d(y) - d(y^*) &= D_1(y) + D_2(y) \\ &\geq D_2(y) \\ &\geq \frac{\sigma}{2}\|x(y) - x^*\|^2, \end{aligned}$$

which is the desired inequality. ■

We now have all the ingredients for proving Theorem 4.6.

Proof of Theorem 4.6. The proof is a direct consequence of Lemma D.1. It can be obtained by setting $A \equiv \boldsymbol{M}$, $f(y) \equiv \|y - \boldsymbol{p}\|_1$, and $g(x) \equiv \alpha\mathcal{E}(x) + \chi_{\Delta_m}(\boldsymbol{\pi})$, with χ_{Δ_m} the indicator function of the set Δ_m. Thus $p(x) = f(Ax) + g(x) = F_\alpha(x)$ and $d(y) = J_\alpha(y)$. Then note that $\boldsymbol{\pi}_k$ defined in Theorem 4.6 satisfies $\boldsymbol{\pi}_k = \nabla g^*(-A^*\boldsymbol{y}_k)$. By Proposition 4.2, we get that g is $\alpha\sigma_{\mathcal{E}}$-strongly convex w.r.t. $\|\cdot\|_{\ell^p}$ for all $p \in [1;\infty]$. It then suffices to use bound (12) together with Lemma D.1 to conclude. ■

Acknowledgments. The authors wish to thank Jean-Baptiste Hiriart-Urruty, Fabrice Gamboa, and Alexandre Vignaud for fruitful discussions. They also thank the referees for their remarks, which helped clarify the paper.

REFERENCES

[AHPR13] B. Adcock, A. C. Hansen, C. Poon, and B. Roman, *Breaking the coherence barrier: Asymptotic incoherence and asymptotic sparsity in compressed sensing*, arXiv:1302.0561, 2013.

[BBW13] J. Bigot, C. Boyer, and P. Weiss, *An analysis of block sampling strategies in compressed sensing*, arXiv:1310.4393, 2013.

[BC11] H. H. Bauschke and P. L. Combettes, *Convex Analysis and Monotone Operator Theory in Hilbert Spaces*, Springer, New York, 2011.

[CCKW13] N. Chauffert, P. Ciuciu, J. Kahn, and P. Weiss, *Variable density sampling with continuous sampling trajectories*, arXiv:1311.6039, 2013.

[CCW13] N. Chauffert, P. Ciuciu, and P. Weiss, *Variable density compressed sensing in MRI. Theoretical vs. heuristic sampling strategies*, in Proceedings of the IEEE International Symposium on Biomedical Imaging, IEEE Press, Piscataway, NJ, 2013.

[CDV10] P. L. Combettes, Đ. Dũng, and B. C. Vũ, *Dualization of signal recovery problems*, Set-Valued Var. Anal., 18 (2010), pp. 373–404.

[CP11a] E. J. Candès and Y. Plan, *A probabilistic and ripless theory of compressed sensing*, IEEE Trans. Inform. Theory, 57 (2011), pp. 7235–7254.

[CP11b] P. L. Combettes and J.-C. Pesquet, *Proximal splitting methods in signal processing*, in Fixed-Point Algorithms for Inverse Problems in Science and Engineering, Springer, New York, 2011, pp. 185–212.

[CRCP12] R. W. Chan, E. A. Ramsay, E. Y. Cheung, and D. B. Plewes, *The influence of radial undersampling schemes on compressed sensing reconstruction in breast MRI*, Magn. Reson. Med., 67 (2012), pp. 363–377.

[CRT06] E. J. Candès, J. Romberg, and T. Tao, *Robust uncertainty principles: Exact signal reconstruction from highly incomplete frequency information*, IEEE Trans. Inform. Theory, 52 (2006), pp. 489–509.

[CT93] G. Chen and M. Teboulle, *Convergence analysis of a proximal-like minimization algorithm using Bregman functions*, SIAM J. Optim., 3 (1993), pp. 538–543.

[dJ13] A. d'Aspremont and M. Jaggi, *An optimal affine invariant smooth minimization algorithm*, arXiv:1301.0465, 2013.

[Don06] D. Donoho, *Compressed sensing*, IEEE Trans. Inform. Theory, 52 (2006), pp. 1289–1306.

[FP11] J. M. Fadili and G. Peyré, *Total variation projection with first order schemes*, IEEE Trans. Image Process., 20 (2011), pp. 657–669.

[GK13] C. C. Gonzaga and E. W. Karas, *Fine tuning Nesterov's steepest descent algorithm for differentiable convex programming*, Math. Program., 138 (2013), pp. 141–166.

[HPH$^+$11] R. Hummel, S. Poduri, F. Hover, U. Mitra, and G. Sukhatme, *Mission design for compressive sensing with mobile robots*, in Proceedings of the IEEE International Conference on Robotics and Automation (ICRA), IEEE Press, Piscataway, NJ, 2011, pp. 2362–2367.

[HUL96] J.-B. Hiriart-Urruty and C. Lemaréchal, *Convex Analysis and Minimization Algorithms: Part 1: Fundamentals*, Springer, New York, 1996.

[JN08] A. Juditsky and A. S. Nemirovski, *Large deviations of vector-valued martingales in 2-smooth normed spaces*, arXiv:0809.0813, 2008.

[KW12] F. Krahmer and R. Ward, *Stable and robust sampling strategies for compressive imaging*, IEEE Trans. Image Process., 23 (2014), pp. 612–622.

[LDSP08] M. Lustig, D. L. Donoho, J. M. Santos, and J. M. Pauly, *Compressed sensing MRI*, IEEE Signal Process. Mag., 25 (2008), pp. 72–82.

[LKP08] M. Lustig, S.-J. Kim, and J. M. Pauly, *A fast method for designing time-optimal gradient waveforms for arbitrary k-space trajectories*, IEEE Trans. Med. Imaging, 27 (2008), pp. 866–873.

[Nes05] Y. Nesterov, *Smooth minimization of non-smooth functions*, Math. Program., 103 (2005), pp. 127–152.

[Nes13] Yu. Nesterov, *Gradient methods for minimizing composite functions*, Math. Program., 140 (2013), pp. 125–161.

[NN04] Y. Nesterov and I. E. Nesterov, *Introductory Lectures on Convex Optimization: A Basic Course*, Appl. Optim. 87, Springer, New York, 2004.

[PDG12] A. C. Polak, M. F. Duarte, and D. L. Goeckel, *Performance bounds for grouped incoherent measurements in compressive sensing*, arXiv:1205.2118, 2012.

[PVW11] G. Puy, P. Vandergheynst, and Y. Wiaux, *On variable density compressive sampling*, IEEE Signal Process. Lett., 18 (2011), pp. 595–598.

[Rau10] H. Rauhut, *Compressive sensing and structured random matrices*, Theoret. Found. Numer. Methods Sparse Recovery, 9 (2010), pp. 1–92.

[Roc97] R. T. Rockafellar, *Convex Analysis*, Princeton Landmarks in Math. and Phys. 28, Princeton University Press, Princeton, NJ, 1997.

[SPM95] D. M. Spielman, J. M. Pauly, and C. H. Meyer, *Magnetic resonance fluoroscopy using spirals with variable sampling densities*, Magn. Res. Med., 34 (1995), pp. 388–394.

[Wri97] G. A. Wright, *Magnetic resonance imaging*, IEEE Signal Process. Mag., 14 (1997), pp. 56–66.

[WSK$^+$07] S. Winkelmann, T. Schaeffter, T. Koehler, H. Eggers, and O. Doessel, *An optimal radial profile order based on the golden ratio for time-resolved MRI*, IEEE Trans. Med. Imaging, 26 (2007), pp. 68–76.